

Civil Engineering Journal

(E-ISSN: 2476-3055; ISSN: 2676-6957)

Vol. 11, No. 09, September, 2025



Numerical Assessment of Inter-Pillar Stability in Inclined Ore Bodies for Underground Mining Design

A. Mussin ¹, A. Imashev ¹, G. Yeskenova ¹, A. Matayev ¹, A. Suimbayeva ¹, C. Zhunusbekova ¹, N. Shaike ¹

¹ Abylkas Saginov Karaganda Technical University, Karaganda, 100012, Kazakhstan.

Received 14 May 2025; Revised 08 August 2025; Accepted 16 August 2025; Published 01 September 2025

Abstract

This paper presents a methodology for assessing the stability of stoping chambers and inter-chamber pillars (ICPs) during underground mining of ore bodies with varying dip angles. The objective is to determine optimal parameters for excavation elements (chamber width and pillar spacing) that ensure the stability of the mining system under fractured rock mass conditions. The Zhezkazgan deposit's geomechanical properties were used as the modeling case study. The methodology includes geotechnical core mapping (with RQD, Q-system, and GSI classifications), laboratory strength testing, field—laboratory correlation, and numerical modeling using the finite element method. Particular focus is placed on the sensitivity of stability to variations in GSI, depth, and excavation geometry. The results indicate that increasing the dip angle significantly reduces the stability of both chambers and pillars. The novelty of this study lies in the comprehensive assessment of structural factors and excavation geometry on mass stability under site-specific geological conditions.

Keywords: Room-and-Pillar Mining System; Inter-Chamber Pillars; Barrier Pillars; Stress-Strain State; Stability; Mineral Loss.

1. Introduction

Underground mining is a complex, multi-stage process that requires detailed consideration of geological and engineering factors. One of the key elements ensuring operational safety and efficiency is the implementation of structural stability measures before the commencement of mining. The feasibility of extracting ore beneath existing structures is directly dependent on the mining and geological stability established during the design phase of safety measures. Modern underground mining development demands the adaptation of conventional technological approaches to increasingly complex geological conditions and the depletion of easily accessible reserves. One pressing engineering challenge is the geomechanical justification of chamber-and-pillar mining system parameters for inclined ore bodies with dip angles ranging from 20° to 35°, particularly relevant for regions such as Zhezkazgan in Kazakhstan.

As shown in Figure 1, approximately 32.4% of the ore reserves in the Zhezkazgan deposit lie in inclined bodies with dip angles between 20° and 35°, constituting nearly one-third of the total approved reserves. These reserves are currently classified as temporarily inactive due to the technical challenges and safety risks posed by conventional chamber-and-pillar methods. This highlights the need to adapt existing systems to ensure the safe and efficient recovery of these resources, reduce ore loss, and improve economic viability [1, 2]. The Inclined Chamber and Pillar (ICP) mining method has traditionally been employed in the extraction of shallow and sub-horizontal ore bodies (with dips up to 20°), where the stress state of the rock mass remains relatively stable, and the influence of tangential stresses on pillar stability is

^{*} Corresponding author: a.imashev@ktu.edu.kz; g.eskenova@ktu.edu.kz



doi http://dx.doi.org/10.28991/CEJ-2025-011-09-06

© 2025 by the authors. Licensee C.E.J, Tehran, Iran. This article is an open access article distributed under the terms and conditions of the Creative Commons Attribution (CC-BY) license (http://creativecommons.org/licenses/by/4.0/).

minimal. However, as mining operations transition to deposits with steeper inclinations, the proportion of shear stresses increases substantially. This change in stress regime alters the mechanisms of load redistribution and rock mass failure, necessitating a reassessment and adaptation of key design parameters within the ICP framework [3–5].

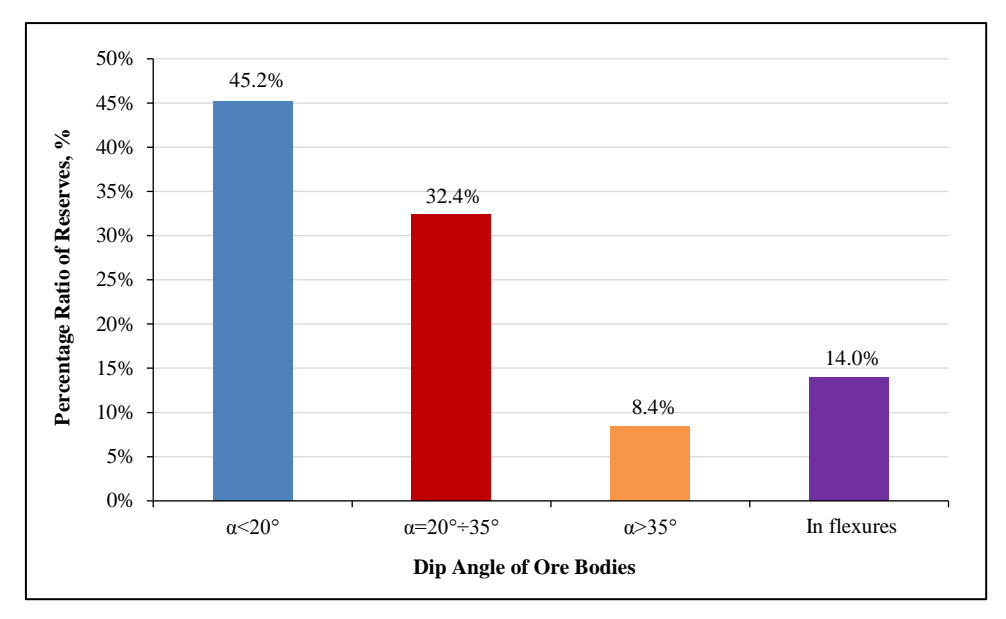


Figure 1. Distribution of ore body reserves of the Zhezkazgan deposit depending on the angles of incidence

Recent international studies underscore the potential for modifying the ICP method to enhance its effectiveness under complex geological and geomechanical conditions. Zhang & Ni (2018), for instance, employed finite element modeling (FEM) to optimize pillar and stope geometries, demonstrating the need for site-specific customization of design approaches based on local stress conditions [5]. Similarly, Napa-García et al. (2019) utilized automated numerical simulations to refine the dimensions of extraction chambers and access ways, thereby minimizing structural failure risks [6].

Contemporary research further supports the necessity of revising ICP parameters. Kumar et al. (2024) investigated the mechanical behavior of coal pillars during sand grouting, reporting a notable improvement in stability due to the presence of fill material [7]. Zhou et al. (2024) applied numerical methods to determine optimal excavation dimensions under variable loading scenarios [8]. Wu et al. (2024) focused on the performance of "roof—coal column" structures in steeply dipping formations, with findings that may also be extrapolated to hard rock settings [9].

The integration of advanced computational tools—such as RS2, RS3, and FLAC3D—has further improved predictive accuracy in modeling stress distribution and deformation patterns in inclined ore bodies [10–13]. These technologies provide a robust basis for developing reliable, adaptive mining strategies in challenging geological environments.

Of particular relevance are studies focusing on the stability of inter-panel pillars. Eremin et al. (2022) demonstrated that in inclined ore bodies, stress concentration within pillars increases significantly, leading to heightened deformation risks [13]. Eremenko et al. (2021) confirmed the necessity of adjusting both pillar height and spacing in salt and polymineral deposits to account for these stress changes [14]. For hard rock conditions, Ma et al. (2016) identified the primary mechanisms of shear failure in pillars subjected to non-standard stress trajectories, underscoring the complexity of pillar response under inclined geometries [15].

In parallel with deterministic numerical approaches, hybrid modeling techniques have gained prominence. Sordo et al. (2024) applied a coupled finite element–material point method (FEM–MPM) framework to capture non-linear deformation behavior in rock masses with complex geometry [16]. Similarly, Quevedo et al. (2024) employed machine learning algorithms to predict pillar failure under chamber mining conditions, marking a significant step toward data-driven geomechanical modeling [17].

A notable contribution to the geomechanical substantiation of chamber-and-pillar mining parameters is provided by Vlachogiannis & Benardos [18], who introduced new analytical expressions for estimating stress distribution in regular pillar configurations. Their study involved extensive two-dimensional and three-dimensional numerical simulations using RS2 and RS3 software (Rocscience Inc.), encompassing a wide range of pillar geometries and mining depths. Based on these simulations, the authors derived empirical formulas for accurately calculating vertical stress within pillars. These results are particularly relevant for the development of inclined ore bodies with dip angles ranging from 20° to 35°, such as those found in the Zhezkazgan mining district. Consequently, the findings of this research are directly applicable to the present study, which aims to optimize ICP system parameters for steeply dipping ore deposits.

A critical review of the analyzed literature reveals several common limitations that hinder the direct application of existing approaches to the mining of inclined ore bodies. First, the majority of studies focus on horizontal or gently dipping deposits, leaving the geometric complexities of ore bodies with dip angles between 20° and 35° insufficiently addressed. Second, existing optimization models for the Inclined Chamber and Pillar (ICP) method typically assume standard excavation parameters, without adequately accounting for stress redistribution in moderately thick rock masses with inclined geometries. Third, a significant portion of the research has been conducted in coal or salt formations, limiting the applicability of the results to hard rock environments such as copper ore deposits, which exhibit markedly different mineralogical and geomechanical characteristics. Moreover, despite the increasing use of advanced numerical modeling techniques, many studies lack in-situ validation or engineering-scale testing, which diminishes their practical relevance and transferability to real-world mining operations.

The approach proposed in the present study addresses these limitations by explicitly adapting to the geological and geomechanical conditions of the inclined copper ore deposits in the Zhezkazgan region. It employs an adaptive numerical modeling framework that incorporates variations in ore body dip angle and depth of occurrence, combined with a comprehensive analysis of the stress–strain behavior of the surrounding rock mass. This integrated methodology enables the development of safe and efficient design parameters for chamber-and-pillar systems in steeply dipping deposits.

The relevance of this research stems from the urgent need to enhance mining efficiency, a priority that becomes particularly critical under conditions of limited natural resource availability. In the current context, the mining industry faces the dual challenge of minimizing ore losses while ensuring both economic viability and environmental sustainability. Addressing this issue aligns with contemporary principles of resource conservation and the rational utilization of mineral resources. The study therefore contributes to the development of mining systems that support sustainable practices without compromising productivity.

The structure of this article is organized as follows: Section 1 provides a comprehensive review of the literature and previous research relevant to the development of chamber-and-pillar mining systems under inclined ore body conditions. Section 2 outlines the research methodology, including the geological framework, numerical modeling tools, and boundary conditions applied in the analysis. Section 3 presents the results of the numerical simulations, followed by engineering interpretations and recommendations for optimizing ICP parameters. Finally, the Conclusion summarizes the key findings and outlines directions for future research. A complete list of references is provided at the end of the article.

2. Research Methodology

Contemporary research on the geomechanics of chamber-and-pillar systems is predominantly grounded in finite element modeling (FEM), which enables detailed simulation of the stress-strain behavior of the rock mass. This approach allows for the incorporation of actual excavation geometries, dip angles, and rock mechanical properties, as well as the development and validation of empirical and analytical formulations that link key design parameters—such as chamber height and width, and pillar width—with anticipated stress levels.

Mehra & Budi (2024) employed nonlinear FEM-based models incorporating the Mohr–Coulomb failure criterion to investigate the influence of rock mass properties and stope geometry on pillar stability under inclined deposit conditions. Their study identified optimal chamber dimensions that minimize plastic deformation and stress concentration [19]. Maina & Konietzky (2025) proposed an analytical correlation based on an extended Hoek–Brown strength criterion that incorporates the mean principal stress component. This model provided a more accurate estimation of the stress distribution within the stope compared to traditional empirical approaches [20].

These two approaches—numerical modeling and analytical formulation—represent the most effective balance between computational accuracy and practical applicability in the context of inclined ore body mining. In contrast, hybrid techniques (e.g., FEM combined with material point methods) and machine learning algorithms, while offering advanced capabilities for analyzing nonlinear and time-dependent deformation processes, remain computationally intensive and require complex calibration procedures. As a result, their current applicability to routine mine design remains limited.

To conduct this study, a structured methodology was developed (Figure 2) to investigate the stress-strain behavior of the rock mass in the context of a chamber-and-pillar mining system applied to inclined ore bodies with dip angles of up to 35°. The approach follows a stepwise procedure, beginning with the collection of baseline geological and geomechanical data and culminating in numerical modeling and engineering interpretation of the results. Each stage of the methodology is logically interconnected, enabling a coherent transition from the physical and mechanical characterization of the rock mass to the derivation of engineering recommendations regarding the stability and design of underground excavations. This integrated framework ensures that the modeling outputs are grounded in realistic input parameters and directly inform practical design decisions.

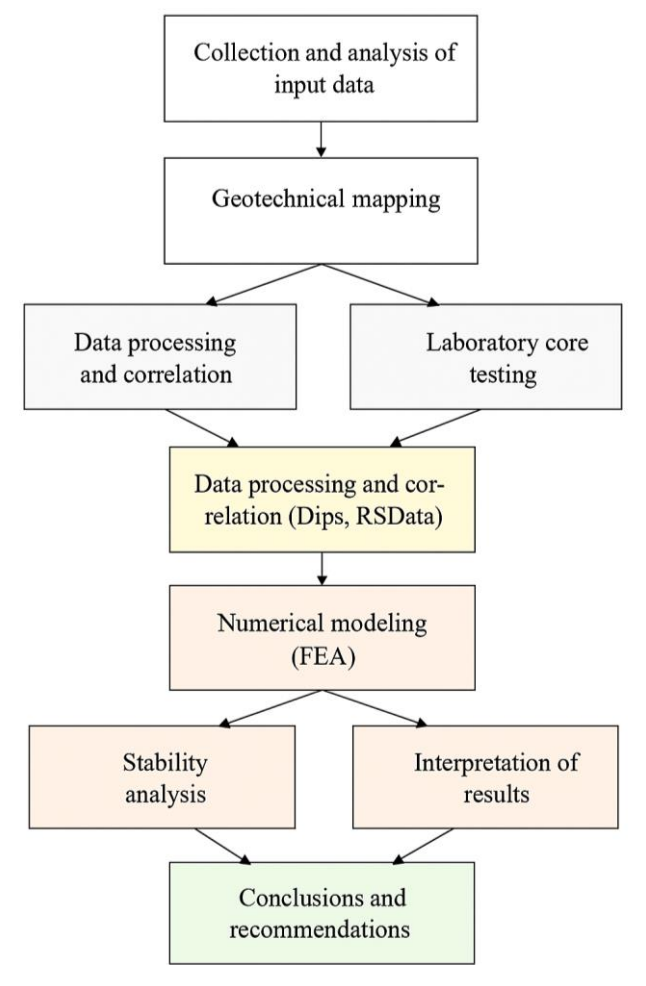


Figure 2. Block diagram of the research stages

At the initial stage of the study, a comprehensive collection, systematization, and preliminary analysis of geological and geotechnical data were performed. This included lithological and stratigraphic information, drilling logs and exploration borehole descriptions, as well as data on tectonic structures, fracturing intensity, and hydrogeological conditions. The integration of these datasets enabled the development of a complete geological model of the deposit and facilitated the identification of key factors influencing the stability of the rock mass.

Detailed geotechnical mapping of accessible mining areas was conducted to assess the structural and mechanical condition of the rock mass. In accordance with the standards of the International Society for Rock Mechanics (ISRM) [13], classification systems such as the Q-System and the Geological Strength Index (GSI) were applied [14]. Field investigations included measurements of joint spacing and orientation, block size, surface roughness, and weathering or alteration of discontinuity surfaces. All field data were systematically recorded in both graphical and tabular formats for subsequent use in numerical modeling. In parallel with field investigations, laboratory testing of rock core samples was conducted to determine representative mechanical properties under natural in situ conditions. Samples were extracted from various geomechanical zones of the rock mass and subjected to a full suite of tests, including uniaxial and triaxial compressive strength, direct shear strength, Young's modulus, Poisson's ratio, and failure strain. The Hoek–Brown failure criterion was also employed to characterize the strength envelope of the rock mass and evaluate stress–strain behavior under varying confining pressures [21-24].

Post-processing of the field and laboratory data was carried out using specialized software packages. Structural data were analyzed in *Dips* to assess fracture orientation and spatial variability, while laboratory strength data were processed in *RSData* to generate strength envelopes and derive input parameters for subsequent numerical simulations.

The *Dips* software was employed to determine the average parameters of fracture systems and to analyze key structural features including Joint Spacing, Rock Quality Designation (RQD), and Joint Frequency. During data processing, the shear condition coefficients JrJ_rJr and JaJ_aJa were calculated; these parameters are critical inputs for assessing rock mass stability using the Barton Q-system. The integration of these analytical tools enables a comprehensive structural-geological and geomechanical characterization of the rock mass.

Figure 3 presents a stereographic projection generated in *Dips*, illustrating the fracture orientation distribution within the rock mass. The plot displays the poles to fracture planes and spatial concentration contours computed by the Fisher method [25], utilizing a counting circle size of 1.0%. The density of pole distribution is visualized using a color scale ranging from 0.0% to 13.0%, with the highest concentration reaching 12.92%. Three predominant fracture sets were identified, characterized by their average dip angles and strike directions. The analysis incorporated 1,827 vectors, weighted according to Terzaghi's method [26], with a minimum displacement angle threshold of 15°.

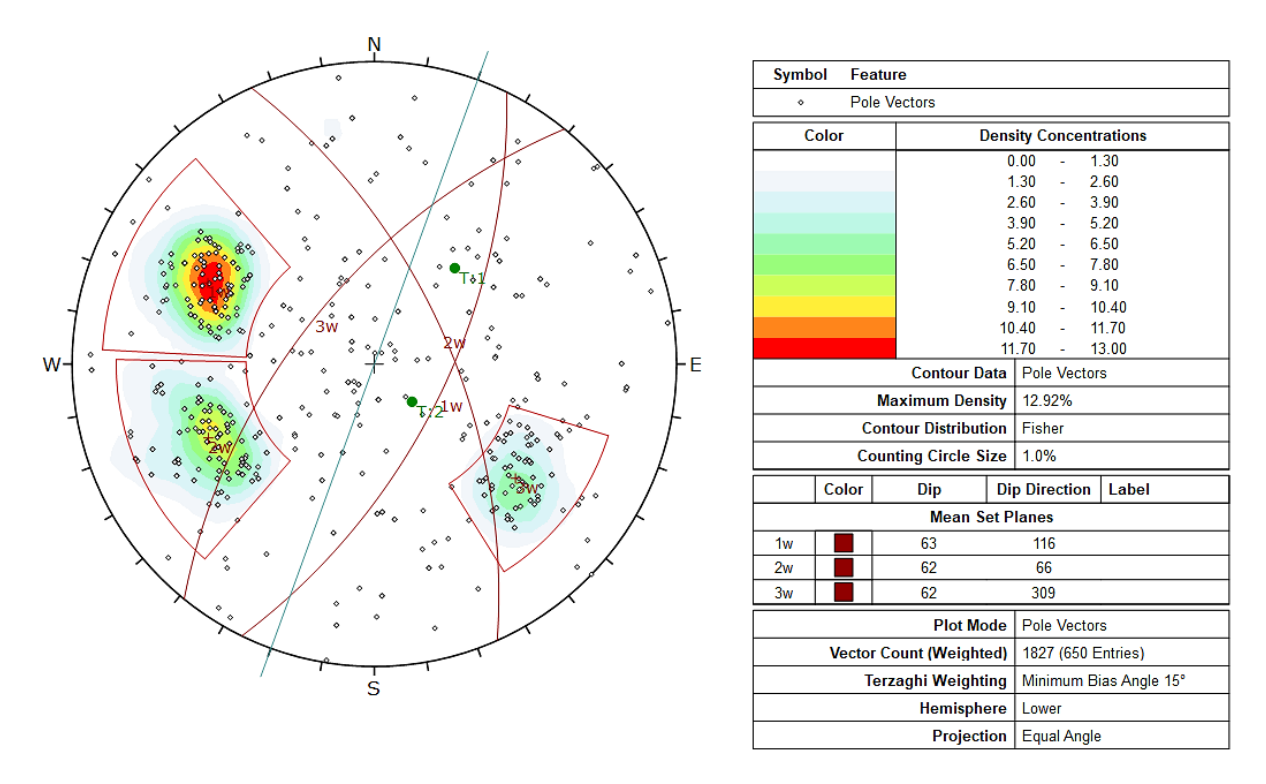
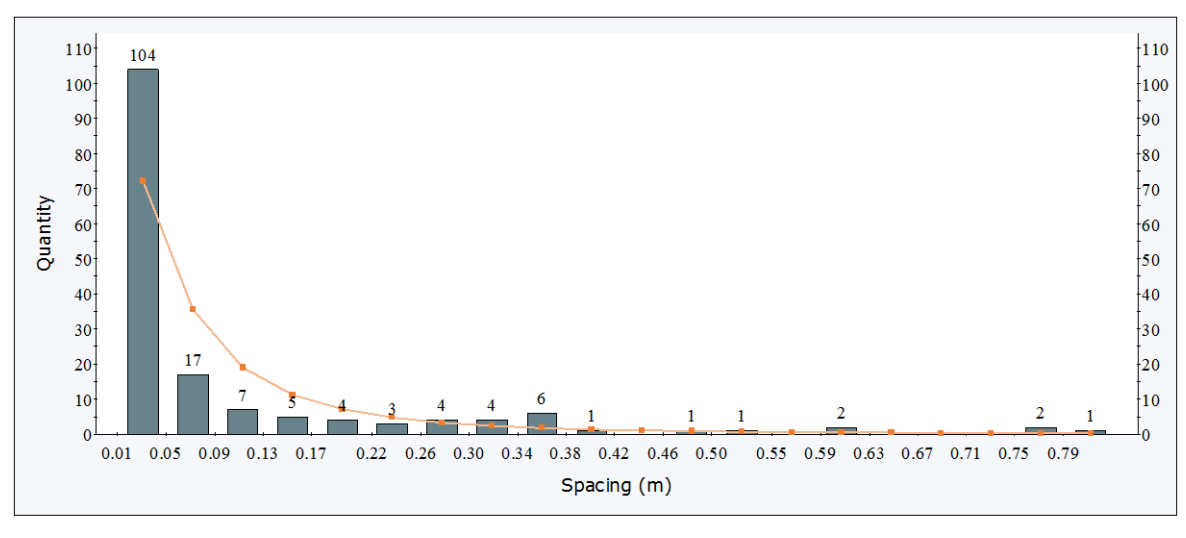


Figure 3. Stereographic projection of fracturing with identification of dominant systems

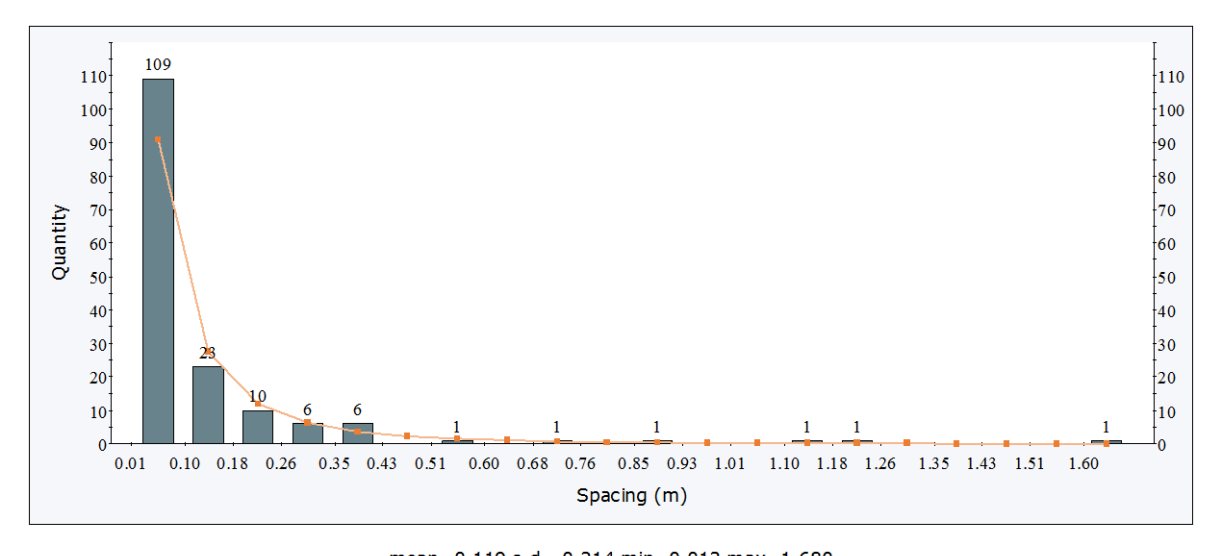
The obtained fracture data serve as essential input parameters for subsequent geomechanical modeling, including the evaluation of rock mass stability via the Barton Q-method [27].

Figures 4 to 6 present histograms illustrating the distribution of True Joint Spacing, calculated based on data from all surveyed drill trails.



 $mean=0.103 \; s.d.=0.153 \; min=0.010 \; max=0.833 \\ FIT: \; LOGNORMAL \; mean=0.103 \; s.d.=0.1537 \; min=0.01035 \; max=0.8334 \\$

Figure 4. Distribution of true joint spacing for the first fracture system (Set 1)



mean=0.119 s.d.=0.214 min=0.013 max=1.680 FIT: LOGNORMAL mean=0.1188 s.d.=0.215 min=0.01294 max=1.68

Figure 5. Distribution of true joint spacing for second system (Set 2)

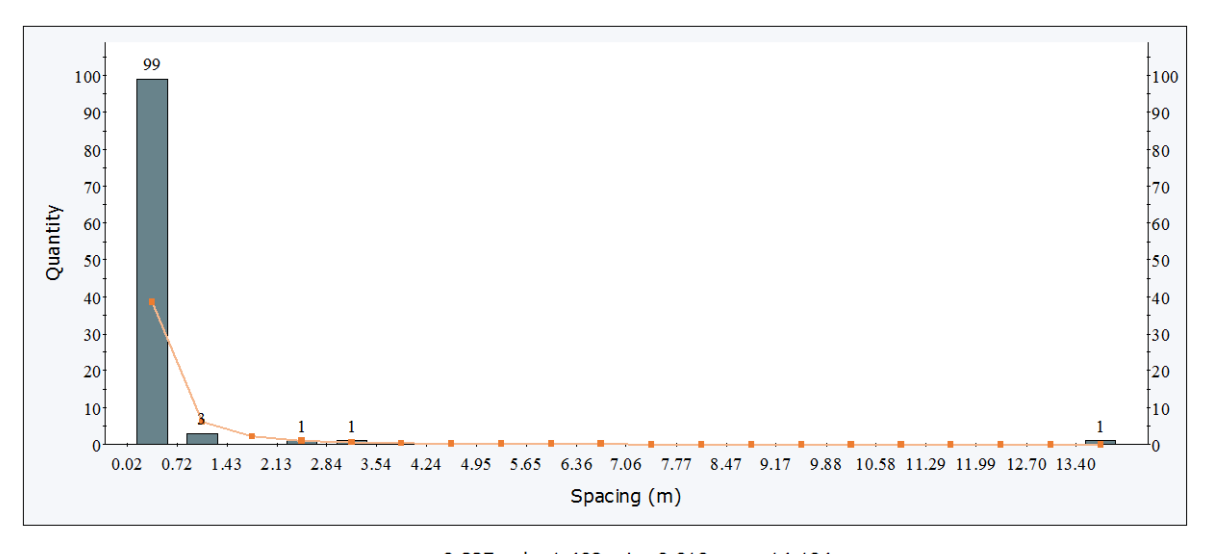


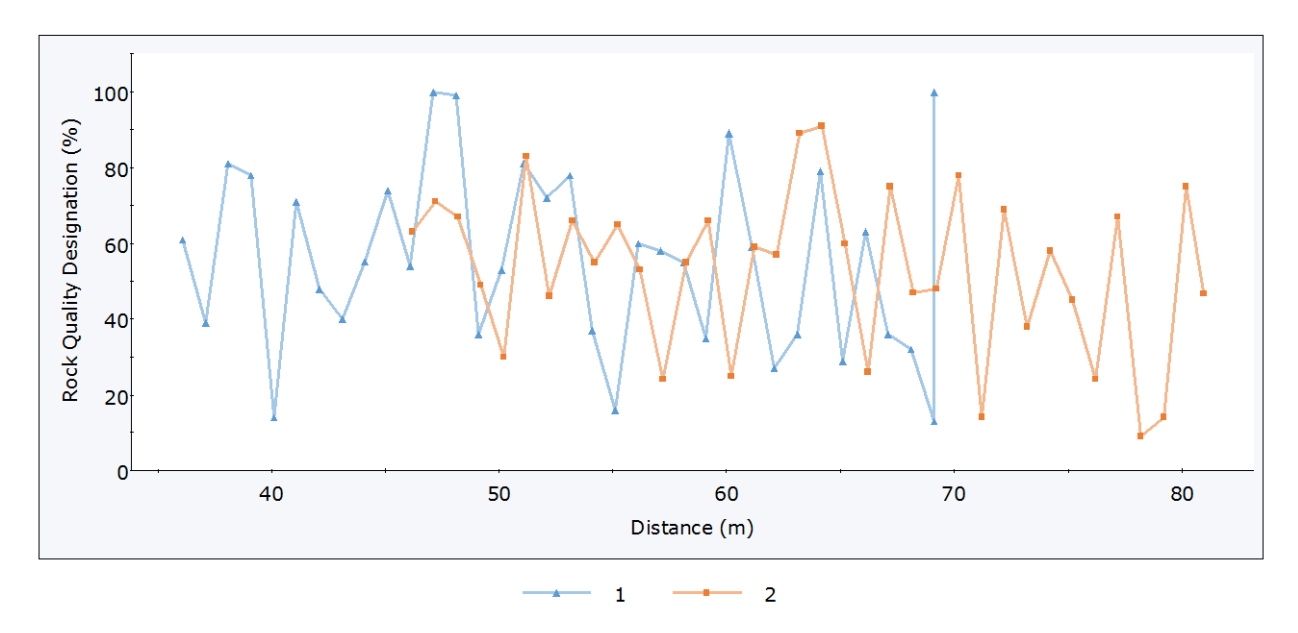
Figure 6. Distribution of true joint spacing for the third fracture system (Set 3)

As part of the structural and geological analysis, histograms of True Joint Spacing distributions were constructed for three distinct fracture systems—Set 1, Set 2, and Set 3—using comprehensive data from all traverses. This analysis provides an objective assessment of the spatial spacing of fractures within the rock mass. The calculated joint spacing coefficient Jn was determined to be 9.

Each histogram displays the joint spacing along the abscissa axis, while the frequency of observations is presented on the ordinate axis. Accompanying each histogram is a lognormal distribution fit, which provides a more accurate representation of the inherently asymmetric distribution typical of natural fractures—characterized by a predominance of small spacing values and the occurrence of less frequent, larger intervals. The analysis of true joint spacing is a critical step in characterizing the rock mass structure and is utilized in the calculation of the joint number coefficient Jn within Barton's Q-system.

Figure 7 presents a line diagram illustrating the Rock Quality Designation (RQD) results for all traverses. The abscissa axis represents the distance along the observation line (in meters), while the ordinate axis shows RQD values expressed as percentages (%). Two colored lines correspond to different routes, conventionally labeled as Traverse 1 and Traverse 2.

The analysis revealed a wide range of RQD values, varying from 9% to 100%, with a mean value of 54.45% and a standard deviation of 22.73%, indicating a high degree of heterogeneity within the rock mass. Fluctuations in RQD reflect alternating zones of heavily fractured, moderately, and well-cemented rock, which are critical considerations in the design of underground workings and the selection of support systems.

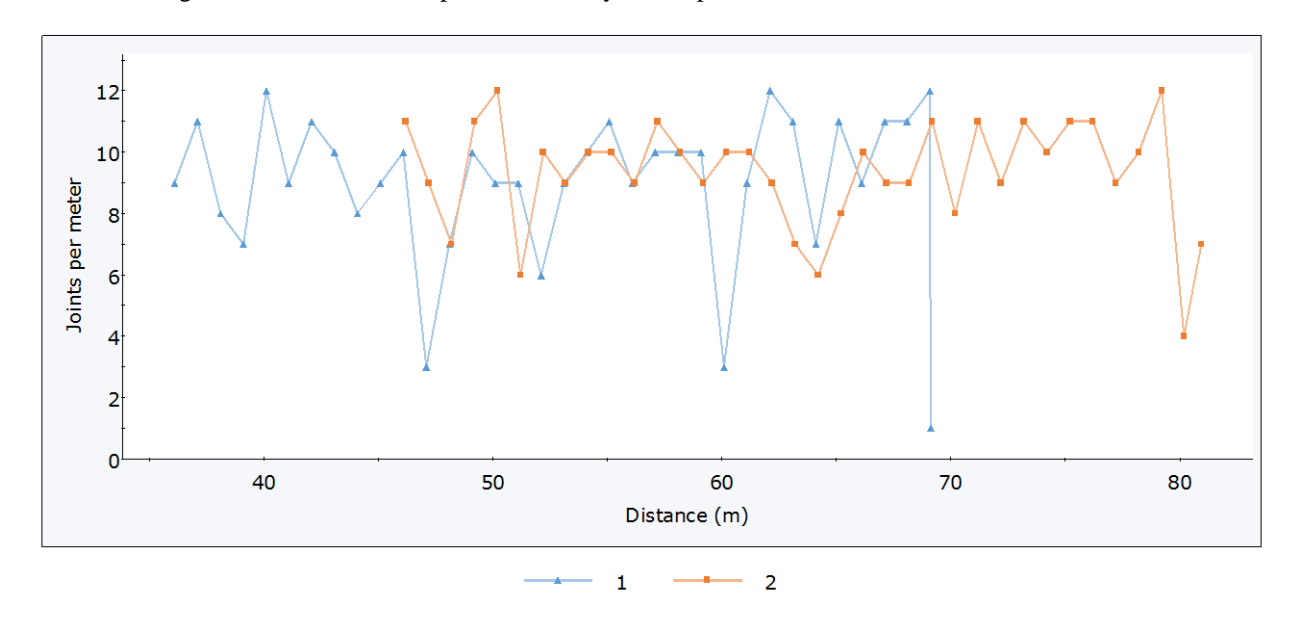


mean=54.446 s.d.=22.730 min=9.000 max=100.000

Figure 7. Distribution graph of the Rock Quality Designation (RQD)

Low RQD values (below 25%) correspond to zones of increased fracturing and weakening of the rock mass, whereas values above 75% indicate good rock quality. This analysis facilitates preliminary classification of engineering and geological conditions along the traverses and informs the stability rating of the rock mass within Barton's Q-system, where RQD is a fundamental input parameter.

Figure 8 presents a line diagram depicting the results of Joint Frequency Analysis derived from data across all traverses. The abscissa axis represents distance along the traverse (in meters), and the ordinate axis indicates joint frequency expressed as joints per meter. Data for two distinct routes (designated as Traverse 1 and Traverse 2) are shown, allowing for assessment of the spatial variability of this parameter.



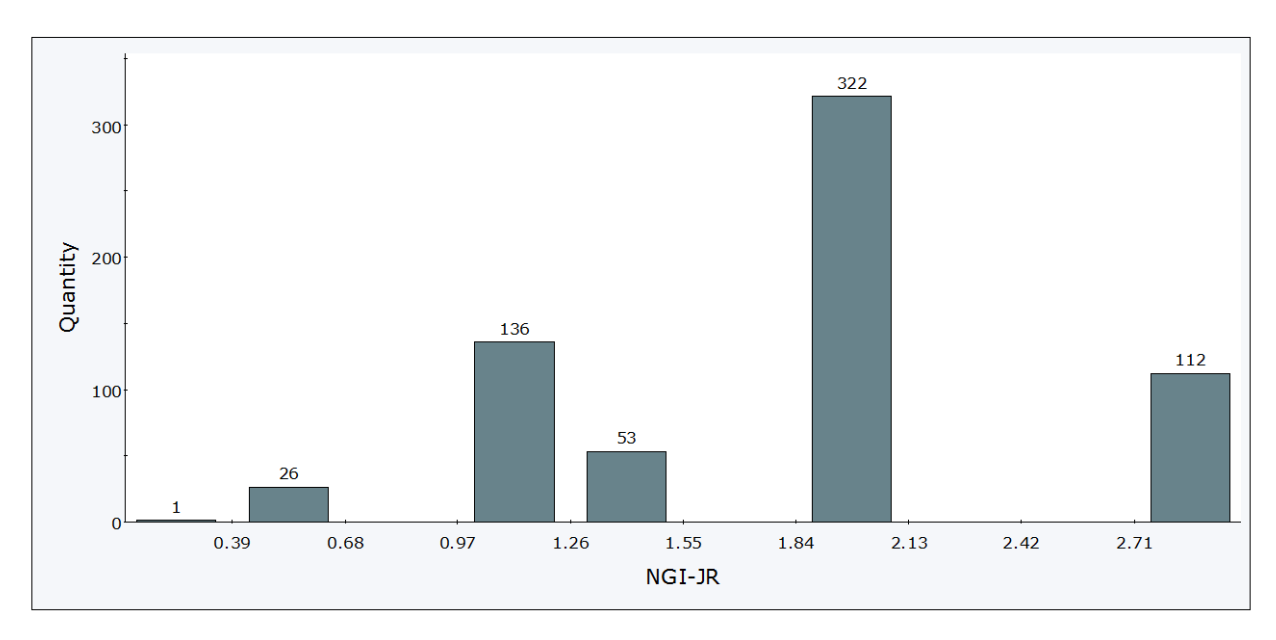
mean=9.155 s.d.=2.173 min=1.000 max=12.000

Figure 8. Fracture frequency distribution

The results demonstrate a high degree of rock mass fragmentation, with an average joint frequency of 9.16 joints/m, characteristic of highly fractured rock masses and indicative of potentially challenging conditions for underground excavation.

Joint frequency is a key parameter in the evaluation of engineering and geological conditions and is incorporated into several geomechanical classification systems, including Barton's Q-method, where it serves as a complementary criterion alongside RQD and J_n .

Figure 9 presents a histogram illustrating the quantitative distribution of the crack surface roughness coefficient (Jr), a key parameter in Barton's Q-method used to assess fracture shear conditions. This coefficient characterizes the mechanical properties of fracture surface contacts and significantly influences the stability of the rock mass under shear displacements.

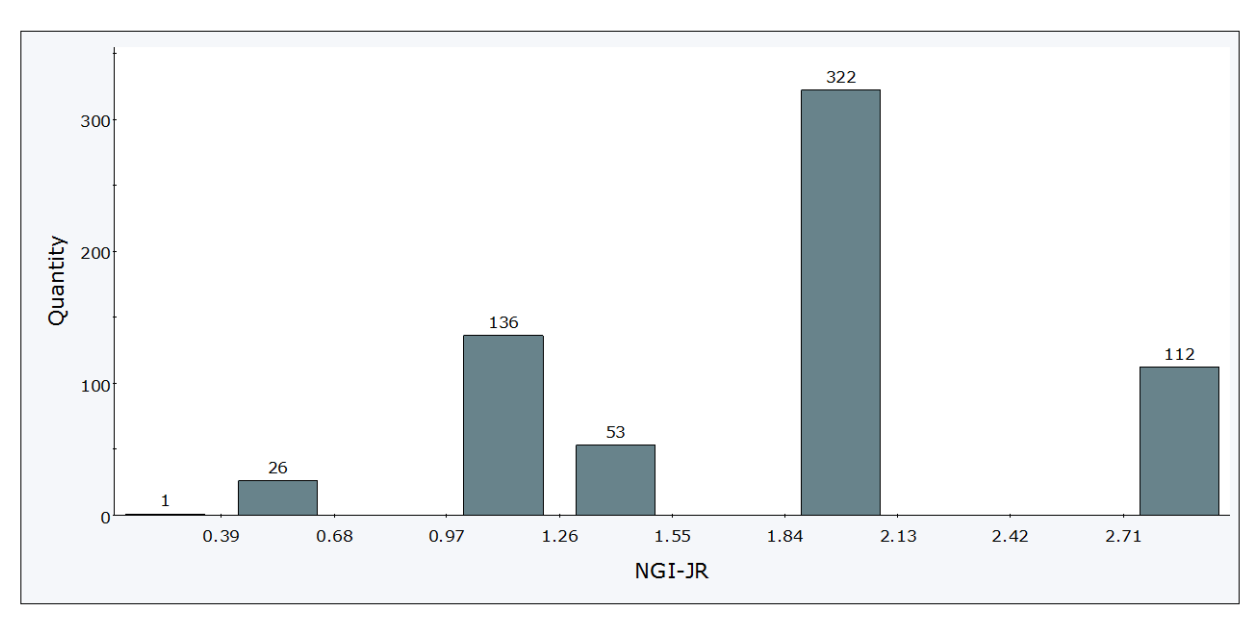


mean=1.85938 s.d.=0.691694 min=0.1 max=3

Figure 9. Histogram of the distribution of the crack roughness coefficient Jr

The highest frequency of observations occurs within the range of 1.84–2.13, with 322 recorded instances. The average value of the Jr coefficient is 1.86, with a standard deviation of 0.69, a minimum value of 0.1, and a maximum of 3.0. This distribution indicates a predominance of fractures exhibiting medium to high roughness, which potentially enhances rock mass stability by increasing shear resistance.

Figure 10 presents a histogram illustrating the quantitative distribution of the crack surface condition coefficient Ja, based on the Norwegian Geotechnical Institute (NGI) classification. The Ja parameter, also included in Barton's Q-system, reflects the degree of alteration, weathering, or infilling of fracture surfaces, thereby influencing their shear stability.



mean=1.85938 s.d.=0.691694 min=0.1 max=3

Figure 10. Histogram of the distribution of the crack condition coefficient ${\bf Ja}$

A high concentration of Ja values in the range 1.5–2.0 indicates relatively favorable shear conditions, positively influencing the stability of the rock mass. The Ja parameter, representing joint surface condition, is used in the Barton Q-system calculations together with the joint roughness coefficient Jr, forming the Jr/Ja ratio—a key indicator of the mechanical behavior of fracture contacts. In Figure 10, Ja values are plotted along the abscissa axis, while the ordinate axis shows the frequency of observations (Quantity) for each Ja value. The distribution reveals that the majority of data points cluster within the 1.5–2.0 range, corresponding to slightly altered joints with rough or mildly oxidized surfaces. The average Ja value is 2.02, with a standard deviation of 0.94, a minimum of 1, and a maximum of 6.

The comprehensive analysis of the rock mass fracturing parameters includes processing data on the spatial orientation of joints, true joint spacing, Rock Quality Designation (RQD), joint frequency, and surface characteristics (Jr and Ja) based on the Norwegian Geotechnical Institute (NGI) classification. This dataset forms a quantitative description of the rock mass structural properties and enables an objective assessment of its engineering-geological condition. The objective of this study is to establish the initial parameters for calculating the rock mass stability rating using the Barton Q-system, which is critical for underground excavation design, slope stability assessment, support system dimensioning, and rock mass stress-strain modeling. Integrating all these parameters provides a robust foundation for subsequent geomechanical calculations and engineering decisions. In the classical Barton Q-system, rock mass condition is evaluated through three fundamental ratios: structural integrity (RQD/Jn), mechanical characteristics (Jr/Ja), and external influences (Jr/SRF). However, in specific cases—such as highly weathered or disturbed rock masses, or when hydrogeological and stress factors have minimal impact—a modified stability index Q' (Q-prime) is recommended, which excludes the Ja and SRF parameters. The formula for the modified Q rating':

$$Q' = (RQD / J_n) \times (J_r / J_a)$$

$$\tag{1}$$

The use of the modified stability index Q' is particularly effective when dealing with highly degraded rock masses where reliable assessment of water saturation or the in-situ stress state is challenging. Under such conditions, the Geological Strength Index (GSI) can be estimated using the following empirical formula. Formula for determining GSI from Q' (Hoek et al.) [28]:

$$GSI = 9 \times ln(Q') + 44 \tag{2}$$

This approach enables the correlation of the rock mass geometric and mechanical characteristics with the Geological Strength Index (GSI) without relying on parameters that are difficult to estimate or may be variable. Therefore, calculating the GSI based on the modified stability index Q' represents a practical and widely accepted alternative to the classical method. It enhances the reliability of engineering-geological assessments, particularly under conditions of limited or unstable information regarding the water saturation and in-situ stress state of the rock mass. As part of the engineering-geological analysis, a modified stability rating Q' was calculated using the Barton system, excluding the effects of water saturation and in-situ stress conditions. Based on the obtained value of $Q' \approx 6.0$, the Geological Strength Index (GSI) was subsequently estimated to be approximately 60.0.

Subsequently, calibration was performed between field measurements and laboratory test results, enabling the extrapolation from localized sample properties to an overall assessment of the rock mass strength characteristics.

Figure 11 presents the calibration results of the rock strength model based on the Mohr–Coulomb failure criterion. The analysis utilizes experimental data on the rock's failure envelope, including principal stresses at fracture. The Levenberg–Marquardt optimization method [29] with absolute vertical error minimization was applied for curve fitting.

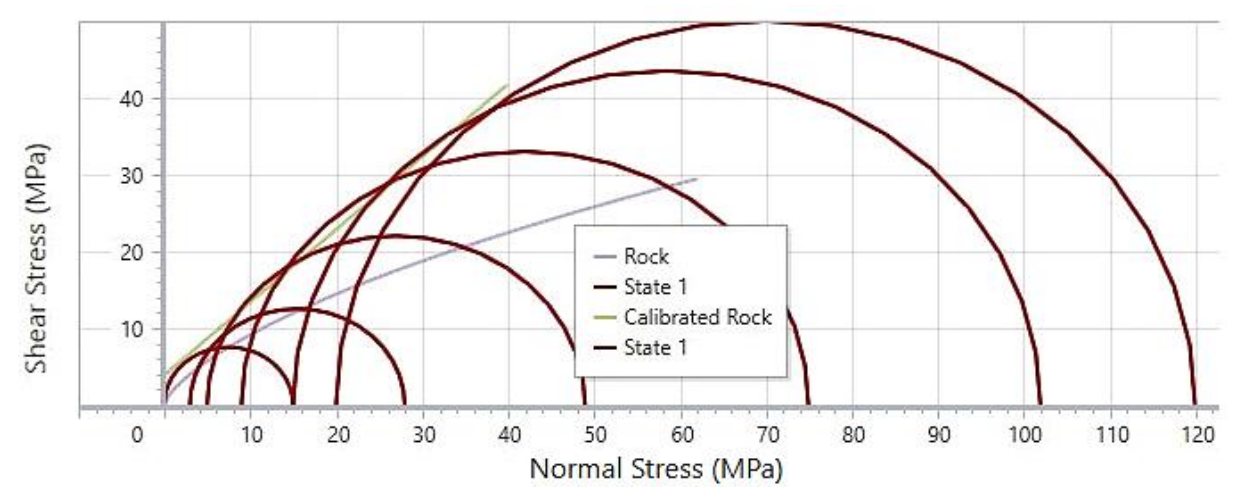


Figure 11. Rock strength data sheet

Figure 11 illustrates the Mohr circles, each representing a failure case at different principal stress levels. The green line denotes the calibrated Mohr–Coulomb failure envelope, which delineates the boundary between stable and unstable states within the normal and shear stress space.

In this study, the strength parameters of the rock mass were compared before and after calibration, with both models described using the Mohr–Coulomb criterion. The calibrated and initial model parameters are summarized in Table 1 for comparison.

Parameter	The Rock Model (Mohr-Coulomb)	Calibrated Rock (Mohr-Coulomb) model
Strength criterion	Mohr-Coulomb	Mohr-Coulomb
Cohesion (C), MPa	10.5	6.6
Friction angle (φ), °	35	31.04
Tensile strength, MPa	0	0
Uniaxial compressive strength, MPa	40.3	23.3
Young's modulus, MPa	19886.5	19.8
Poisson's ratio	0.3	0.3
GSI	60	60
D-factor	0.8	0.8

Table 1. Comparison of Initial and Calibrated Rock Mass Model Parameters

The initial rock mass model exhibits high values of cohesion (10.5 MPa), internal friction angle (35°), and uniaxial compressive strength (40.3 MPa), characteristic of a strong and intact rock mass. Following calibration against field data, these parameters decrease to cohesion of 6.6 MPa, internal friction angle of 31.04°, and compressive strength of 23.3 MPa. This adjustment reflects a more realistic representation of the rock mass behavior under in-situ conditions, enhancing the reliability of subsequent numerical modeling.

Dynamic influences related to mining activities, particularly blasting operations, were incorporated in the numerical simulations. Yue et al. [30] demonstrated that the weakening of mechanical properties due to explosive damage can be quantified by the damage factor (D-factor), which modifies the rock strength parameters. In this study, a conservative maximum damage value of D=0.8 was adopted, corresponding to poor blasting quality and intense dynamic effects. This approach simulates a worst-case scenario in which explosive energy significantly reduces the stability of interchamber pillars, especially in inclined ore body conditions. Although specialized seismodynamic modeling was not conducted, inclusion of the D-factor provides a realistic approximation of the impact of repeated blast loads on excavation stability, allowing identification of critical zones susceptible to failure under combined static and dynamic stresses.

Finite element method (FEM) modeling of the rock mass aimed to delineate zones of inelastic deformation surrounding the mined-out voids. The primary objective was to analyze stress distribution and identify regions at risk of instability, thereby enabling targeted engineering interventions to prevent collapses.

Calculations were performed using the RS2 software by Rocscience, which provides two-dimensional FEM analysis tailored to rock mechanics problems. The modeling applied the Hoek-Brown failure criterion to evaluate the stress-strain response of the rock mass. FEM analysis allowed assessment of stress concentrations, relief zones, displacement patterns, and other key stability indicators.

Based on the numerical simulation outcomes, empirical relationships were derived to optimize chamber widths, permissible dimensions of extraction openings (height and width), and positioning of barrier pillars, aiming to minimize stress concentrations and ensure safe, efficient mining operations.

3. Results and Discussion

The geomechanical characteristics of rocks and ores used in this study were obtained from previously conducted investigations at the Zhezkazgan ore deposit, located in the central part of the Republic of Kazakhstan near the city of Zhezkazgan. The calibrated physical and mechanical parameters of the rock mass, which served as the basis for numerical modeling, are presented in Table 1 (Calibrated Rock Mass Model). In the course of numerical simulations, these parameters were generalized to represent the overall behavior of the rock mass; however, the Geological Strength Index (GSI) was selectively varied. The GSI value is a key input parameter, which significantly influences the calculated stress-strain response of the rock mass in the model.

According to the Technological Regulations for Chamber-and-Pillar Mining with Permanent Pillars applied at the Zhezkazgan underground mine, for the development of inclined ore bodies with dip angles ranging from 20° to 35°,

inter-chamber pillars must be placed with an inclination toward the rise of the deposit. The angle of inclination (β) is defined as half the dip angle (α), that is, $\beta = \alpha/2$, measured relative to the normal to the bedding planes.

In cases of vertically overlapping ore bodies, it is recommended to align the axes of the inter-chamber pillars along the ore body roof to ensure vertical continuity between the support elements (Figure 12). This configuration improves the load-bearing performance of the structure and minimizes the risk of progressive failure across multiple levels.

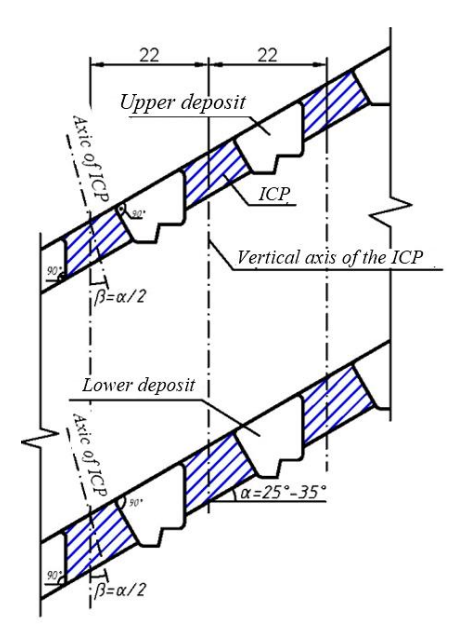


Figure 12. The layout of the inter-chamber pillars during the development of inclined deposits with an angle of incidence of 20°-35°

To substantiate the optimal geometric parameters of the stope chambers and inter-chamber pillars (ISPs), a series of numerical simulations was conducted by varying the widths of the extraction chambers and the separating pillars. The modeling was performed for orebody dip angles of 20°, 25°, 30°, and 35°, reflecting the typical range encountered in the Zhezkazgan deposit.

Within the framework of the simulation, the following key geomechanical indicators were analyzed: Safety Factor (SF) — characterizing the margin of stability of the rock mass in the vicinity of excavation elements; Maximum Principal Stress (σ_1) and Minimum Principal Stress (σ_3) — representing the state of compressive and tensile stress fields in the massif. The spatial distribution of the principal stresses allowed for the identification of zones of stress concentration, where the risk of failure is elevated, as well as stress relief zones, which are typically associated with relaxation and potential deformation.

The formation of these stress zones is a natural consequence of the mining-induced disturbance of the in-situ stress field. As excavation progresses, the rock mass experiences a redistribution of internal stresses — some components of the stress tensor increase beyond their initial natural values (stress concentration), while others decrease (stress relief). These phenomena play a critical role in evaluating the stability of chambers and inter-chamber pillars, particularly under inclined orebody conditions.

3.1. Calculation of the Parameters of the Inter-Chamber Rear Sight

Under the mining and geological conditions of the Zhezkazgan deposit, the layout of inter-chamber pillars is typically designed according to a square grid pattern, with a spacing of 20 meters between the axes. This configuration is selected to minimize the risk of collapse, optimize the utilization of the rock mass, and ensure compliance with safety parameters recommended for the stable development of the deposit.

The design and assessment of inter-chamber pillars were performed using the finite element method (FEM), implemented through high-precision software capable of detailed analysis of the stress-strain state of the rock mass. The simulation aimed to identify zones of inelastic deformation that develop around the stope during its operation. To achieve this, the mechanical properties of the rocks, the geological structure of the massif, and stress conditions associated with ore body development were taken into account.

Additionally, a stability analysis of the inter-chamber backfill (rear sight) was conducted as part of the simulation process. This analysis evaluated its capacity to withstand stresses induced by rock pressure under varying operational conditions, including changes in orebody dip angles, geometric parameters of the backfill, and general mining conditions.

The simulation results facilitated the identification of critical zones within the rock mass that are susceptible to stability loss. Based on this, the dimensions and placement of inter-chamber pillars were optimized to enhance the reliability and safety of mining operations.

Figures 13 to 15 illustrate the results of numerical modeling of the rock mass stress—strain state, performed to assess the influence of different geometric configurations of stope chambers and inter-chamber pillars on rock stability. The simulations were conducted for an ore body with a thickness of 5 meters and a dip angle (α) ranging from 20° to 35°, located at a depth of approximately 400 meters below the surface. Various combinations of stope and pillar geometries were analyzed, including configurations of 11×9 m, 12×8 m, 13×7 m, and 14×6 m, where the first value denotes the width of the stope chamber and the second denotes the width of the inter-chamber pillar.

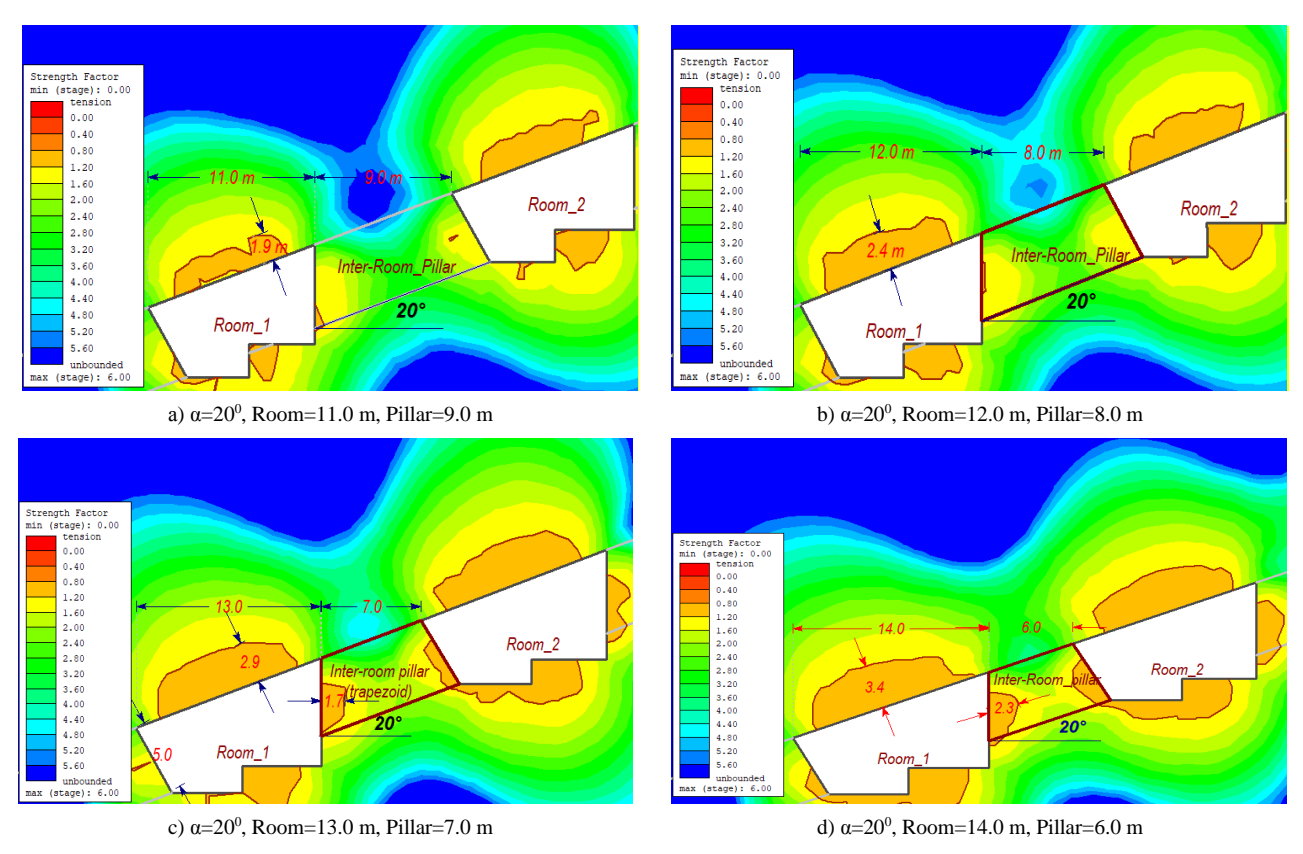


Figure 13. The results of numerical analysis with an ore deposit thickness of m=5 m and an angle of incidence of α =20°

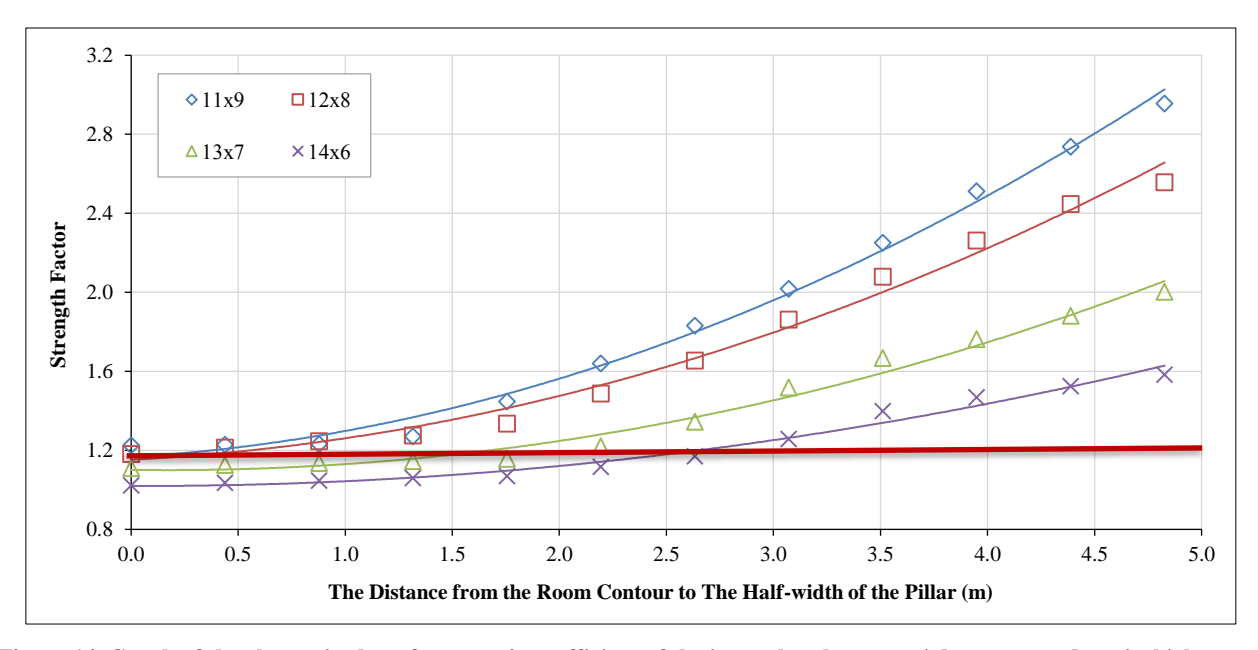


Figure 14. Graph of the change in the safety margin coefficient of the inter-chamber rear sight at an ore deposit thickness of m = 5 m and an angle of incidence of $\alpha = 20^{0}$

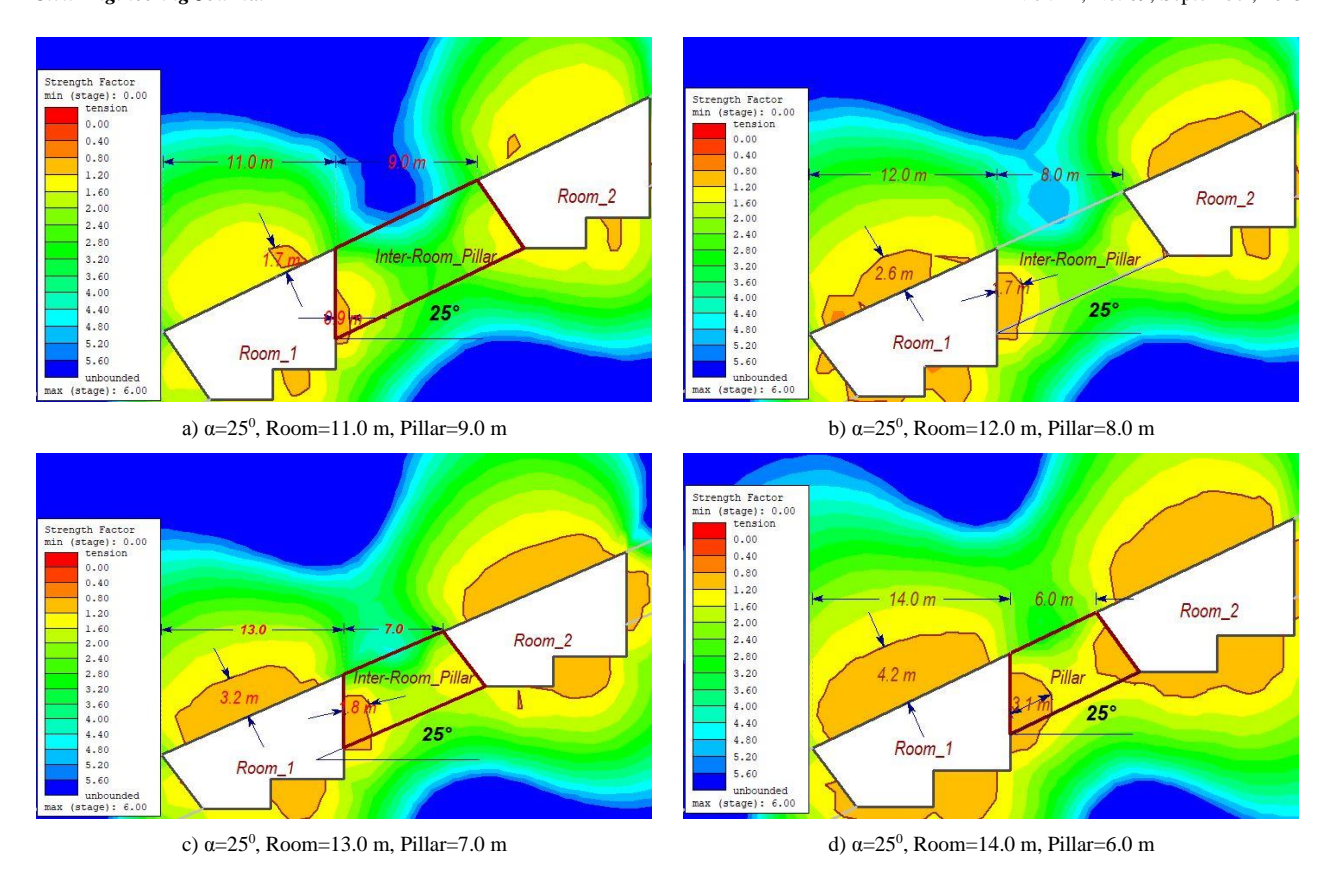


Figure 15. Results of numerical analysis with an ore deposit thickness of m = 5 m and an angle of incidence of α = 25°

The primary focus was on determining key indicators such as the safety factor (SF), as well as principal compressive (σ_1) and tensile (σ_3) stresses. The safety factor was used to evaluate the overall stability of the rock mass and the ability of the chambers and pillars to resist external loads induced by rock pressure. Analysis of σ_1 and σ_3 provided insight into zones of stress concentration and relief within the rock mass—critical for the prevention of structural failure and collapse.

In this study, a Safety Factor (SF) of 1.2 is adopted as the threshold criterion for evaluating the stability of the rock mass. This value corresponds to the minimum acceptable safety level commonly employed in mining and geotechnical engineering for temporary and operational excavations. According to established engineering standards, SF values ranging from 1.2 to 1.5 ensure adequate stability while allowing for the efficient use of resources, whereas SF values exceeding 2 are typically reserved for particularly critical structures that demand a higher reliability margin.

The selection of the threshold SF = 1.2 reflects the need to balance safety considerations with economic efficiency in the design of the chamber-pillar system. This value accommodates potential geotechnical uncertainties and provides a sufficient safety margin to mitigate the risk of collapse under typical underground mining conditions.

Figure 13 presents the results of a numerical analysis of the stress–strain state of the rock mass for different ratios between the widths of the chamber and the inter-chamber rear sight. Four configurations of the chamber-pillar system with varying geometric parameters were examined: (a) chamber width of 11.0 m with a rear sight width of 9.0 m, (b) 12.0 m and 8.0 m, (c) 13.0 m and 7.0 m, and (d) 14.0 m and 6.0 m, respectively.

A safety factor (SF) of 1.2 was adopted as the threshold value for stability assessment, with regions exhibiting SF < 1.2 classified as potentially unstable. In the configurations 11×9 m and 12×8 m, fracture zones were confined primarily to the peripheral contours. In contrast, the 13×7 m configuration—and more prominently the 14×6 m configuration—displayed the development of unstable zones within the inter-chamber rear sight.

Based on these results, the optimal geometric parameters for the system are a chamber width less than 13 m and a rear sight width equal to or greater than 7 m.

Figure 14 illustrates the variation of the safety factor (SF) along the width of the inter-chamber rear sight for the four geometric configurations studied. In the 11×9 m and 12×8 m configurations, SF values predominantly exceed the threshold of 1.2, indicating acceptable stability. Conversely, in the 13×7 m and 14×6 m configurations, a substantial portion of the rear sight fails to meet the stability criterion. The results clearly demonstrate that a reduction in the rear sight width significantly diminishes its load-bearing capacity.

Figure 15 presents the results of numerical simulations for an ore body with a thickness of 5 m and a dip angle (α) of 25°, evaluated for various configurations of chamber widths and inter-chamber pillars. Consistent with previous analyses, a safety factor (SF) of 1.2 was adopted as the critical threshold, with regions exhibiting SF < 1.2 classified as unstable.

Configurations (a) and (b) demonstrate stability across the majority of the rock mass, whereas in configurations (c) and particularly (d), zones of instability significantly expand, encompassing most of the volume of the inter-chamber pillars.

The increase in dip angle to 25° intensifies the development of unstable zones for identical geometric parameters. Notably, even the 12×8 m configuration approaches the stability threshold in substantial edge zones. These findings highlight the heightened sensitivity of the rock massif to variations in the ore body's dip angle and underscore the necessity to revise permissible geometric parameters during mine design to ensure operational safety.

Figure 16 depicts the distribution of the safety factor (SF) from the chamber contour to the center of the interchamber rear sight for four geometric configurations: 11×9 m, 12×8 m, 13×7 m, and 14×6 m.

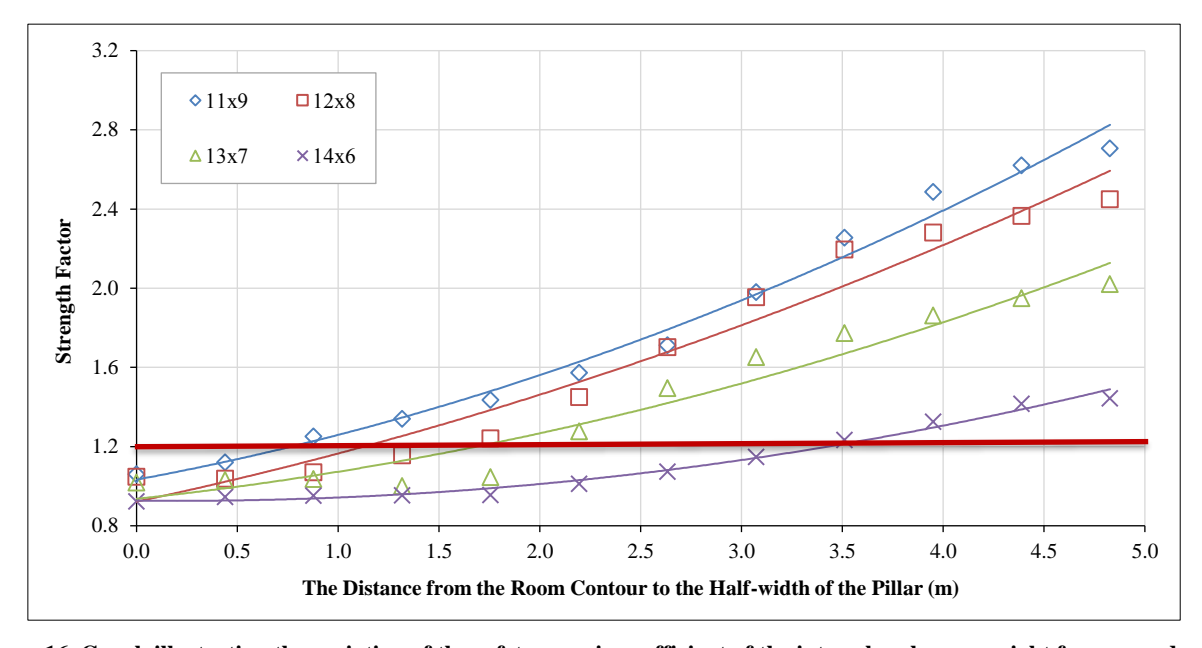
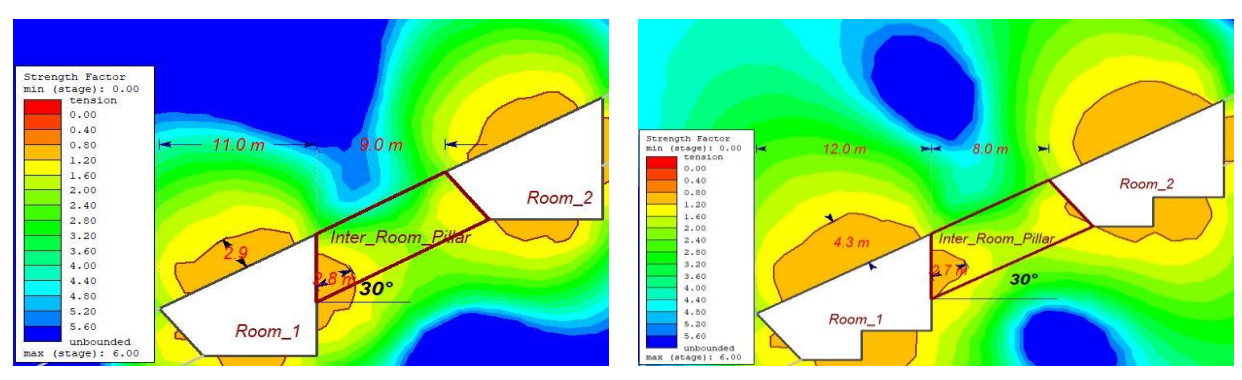


Figure 16. Graph illustrating the variation of the safety margin coefficient of the inter-chamber rear sight for an ore deposit thickness of m=5 m and a dip angle of $\alpha=25^{\circ}$

Consistent with the results obtained at a dip angle of $\alpha=20^\circ$, stability is maintained for the 11×9 m configuration and partially for the 12×8 m configuration. However, in comparison to the previous case, SF values decrease more rapidly and exhibit a flatter, more pronounced downward trend across all configurations. The 13×7 m and 14×6 m configurations fail to reach the critical SF threshold of 1.2 even at the central section of the rear sight, corroborating the simulation results and indicating a high likelihood of plastic deformation and fracturing.

Figure 17 illustrates the distribution of the safety factor (SF) for four chamber-pillar configurations at a dip angle of $\alpha = 30^{\circ}$ and an ore deposit thickness of 5 m. The analysis reveals that, compared to dip angles of 20° and 25° , instability zones significantly expand at $\alpha = 30^{\circ}$, even in the most stable configurations.



a) $\alpha = 30^{\circ}$, Room=11.0 m, Pillar=9.0 m

b) $\alpha = 30^{\circ}$, Room=12.0 m, Pillar=8.0 m

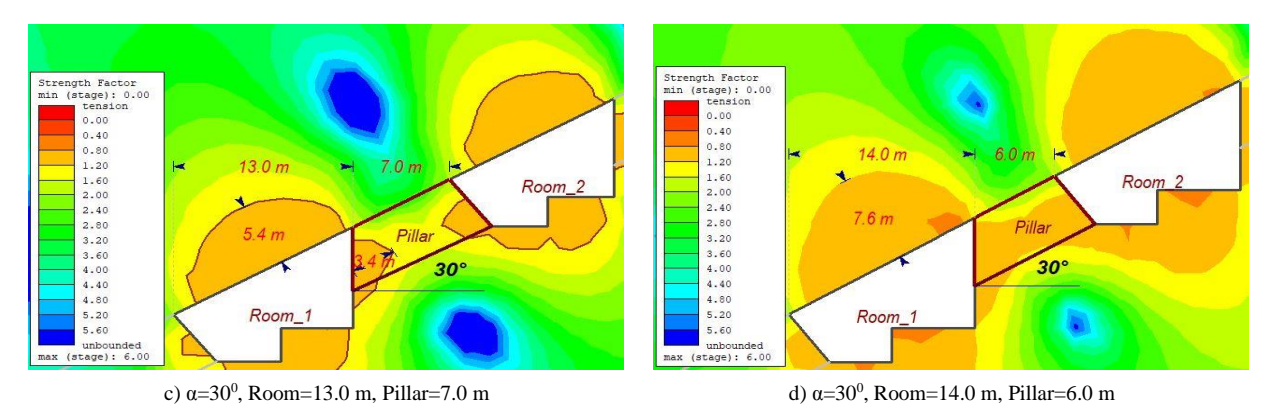


Figure 17. Results of numerical analysis for an ore deposit with a thickness of m = 5 m and a dip angle of $\alpha = 30^{\circ}$

For the 11×9 m configuration, failure zones remain localized at the edges. However, in the 12×8 m and especially the 13×7 m configurations, instability affects a substantial portion of the rear sight. In the 14×6 m configuration, the instability zone (SF < 1.2) nearly overlaps the entire rear sight area, indicating a complete loss of load-bearing capacity. Unlike previous cases, stability decreases more sharply at the same chamber spacing, where even minor reductions in the width of the rear sight cause critical deterioration of the rock mass strength. This behavior is attributed to stress redistribution within the inclined ore body and the activation of shear zones.

The graph presents the distribution of the safety factor (SF) from the chamber contour to the center of the rear sight for four geometric configurations: 11×9 m, 12×8 m, 13×7 m, and 14×6 m. Compared to cases with lower dip angles, the SF values are noticeably reduced across the entire width of the rear sights, particularly in the contour zones. Even for the most stable configuration (11×9 m), the SF at the edges approaches the critical threshold. In the 13×7 m and 14×6 m configurations, a significant portion of the rock mass fails to meet the stability criterion. These results underscore the sharp decline in structural stability with increasing dip angle to 30° , indicating the necessity to revise design parameters by either increasing the width of the rear sight or decreasing the width of the chambers (Figures 19 and 20).

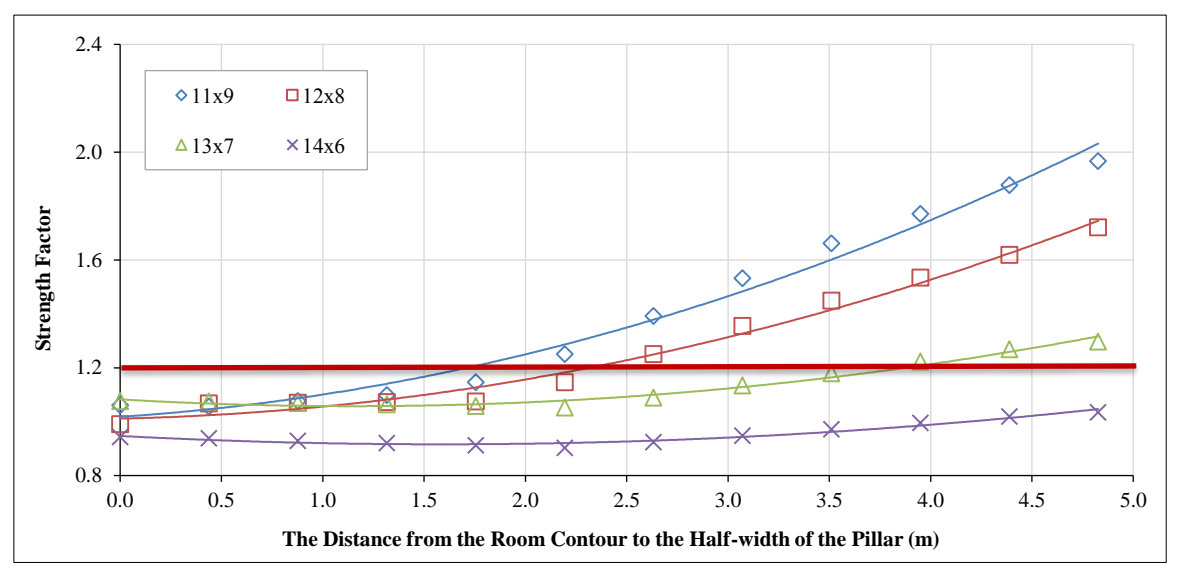


Figure 18. Graph showing the variation of the safety margin coefficient of the inter-chamber rear sight for an ore deposit thickness of m = 5 m and a dip angle of $\alpha = 30^{\circ}$

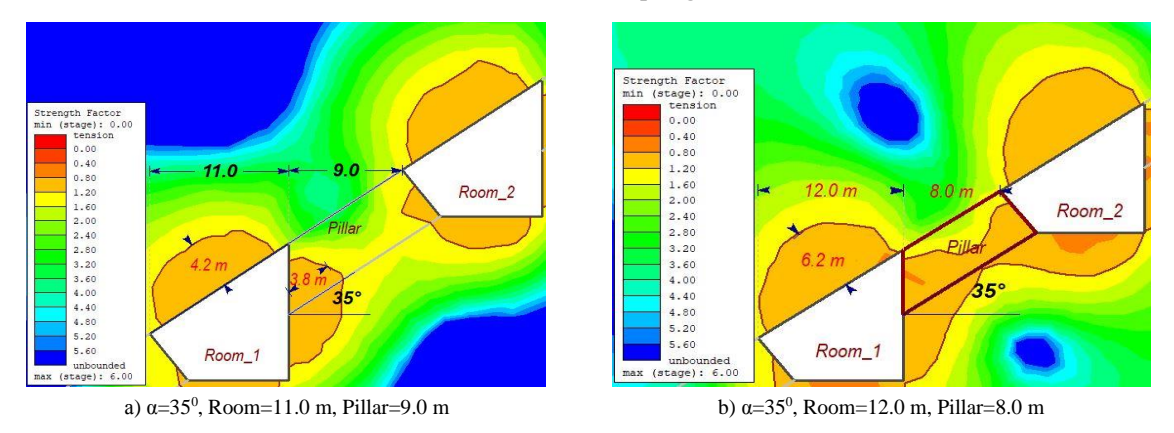


Figure 19. Results of numerical analysis for an ore deposit with a thickness of m = 5 m and a dip angle of $\alpha = 35^{\circ}$

The Figure presents the results of numerical modeling of rock mass stability at an ore body dip angle of $\alpha = 35^{\circ}$ and a thickness of 5 m. Two design geometry variants are analyzed:

- (a) Chamber width of 11.0 m and rear sight width of 9.0 m;
- (b) Chamber width of 12.0 m and rear sight width of 8.0 m.

A safety factor (SF) threshold of 1.2 was applied, with zones exhibiting SF < 1.2 considered potentially unstable. In configuration (a), instability zones are confined to the marginal areas of the rear sight and do not extend into its central region. Conversely, in configuration (b), the SF < 1.2 zone expands considerably, encompassing the majority of the inter-chamber rear sight and indicating a high likelihood of structural failure.

The increase in dip angle to 35° demonstrates that even a moderate reduction in rear sight width results in a significant loss of stability. These findings suggest that conventional chamber-pillar system parameters become ineffective under such conditions, warranting the consideration of alternative mining development methods.

Figure 20 illustrates the variation of the safety factor (SF) along the width of the inter-chamber rear sight for two configurations: 11×9 m and 12×8 m. In the 11×9 m configuration, SF values remain above the critical threshold of 1.2 throughout most of the cross-section, indicating adequate stability. Conversely, in the 12×8 m configuration, SF falls below 1.2 across the entire rear sight width, particularly in the contour zone where it approaches critically low values of approximately 0.8.

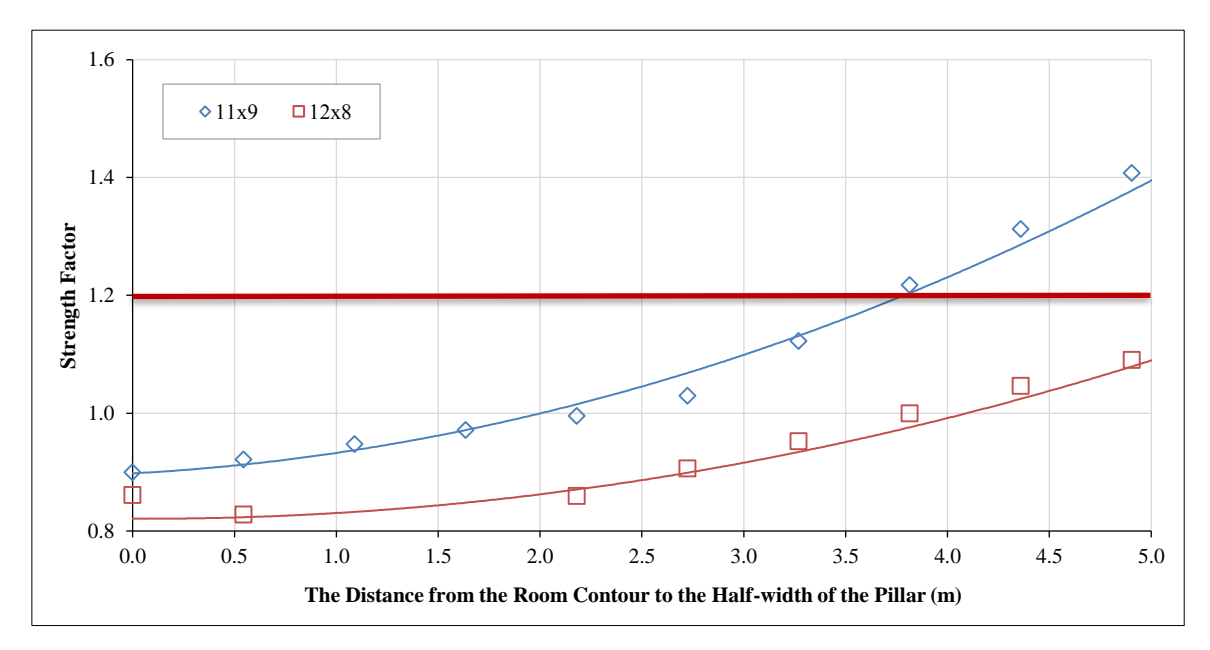


Figure 20. Graph of the change in the safety margin coefficient of the inter-chamber rear sight at an ore deposit thickness of m = 5 m and an angle of incidence of $\alpha = 35^{\circ}$

Based on numerical modeling of the chamber-pillar system stability with varying chamber and inter-chamber pillar configurations, as well as changes in ore body dip angle from 20° to 35°, important design patterns have been established for underground workings.

The results of numerical simulations of the rock mass stress–strain state for ore deposits with dip angles of 20° , 25° , 30° , and 35° (Figures 13, 15, 16, and 19) demonstrate the significant influence of excavation geometry and structural-geological conditions on the stability of inter-chamber pillars (ICP). Four typical configurations were analyzed: 11×9 m, 12×8 m, 13×7 m, and 14×6 m, where the first value represents the width of the cleaning chamber and the second the width of the ICP.

The strength factor (SF) was used as the stability criterion, with a threshold value of SF = 1.2 adopted in accordance with engineering standards as the minimum allowable level for stable mine operation under mining loads. Zones with SF < 1.2 were interpreted as areas of probable stability loss.

Visualization of deformation zones revealed that a reduction in the width of the cleaning chamber (MCC) leads to an increase in the volume of inelastic deformation and the formation of stress concentrators, especially near the contours. Moreover, for fixed geometric parameters, an increase in the ore body dip angle results in the expansion of fracture zones in the chamber roof and within the rear sight.

This trend is evident in the SF distribution graphs (Figures 14, 16, 18, and 20), where SF values decrease with increasing dip angle and decreasing rear sight width. For example, at a dip angle of 20° and excavation dimensions of

 12×8 m, the zone of instability along the chamber roof does not exceed 2.4 m, and the ICP remains stable (SF > 1.2). However, with similar geometry at a dip angle of 35° , the roof collapse zone extends to 4.2 m, and the inter-chamber rear sight is critically unstable, with SF < 1.0 over most of its cross-section.

Numerical modeling has demonstrated that with an increase in the dip angle of the ore body, not only does the depth of stress influence change, but also the pattern of stress distribution alters significantly. Stress concentrations intensify near the edge zones of the chamber, which promotes localization of damage and consequently reduces the overall stability of the chamber-pillar system.

The stability of the chamber-pillar system during underground mining of ore bodies is governed by a complex interplay of factors, among which the ore body's dip angle is of critical importance. The results obtained underscore the necessity for adaptive design of excavation geometry that accounts for local geological conditions, with numerical modeling serving as an indispensable component of the engineering assessment process.

It should be emphasized that all calculations were performed using geotechnical and geological data specific to the Zhezkazgan deposit. The geomechanical parameters considered—including the Geological Strength Index (GSI), insitu stress state, and lithological characteristics—reflect the unique conditions of this particular mining site. Therefore, it is essential to note that the modeling results are site-specific and must be carefully adapted when applying the methodology to other mining and geological environments.

To evaluate the robustness of the model and the generalizability of the findings, a sensitivity analysis was conducted on key parameters influencing the stability of inter-chamber pillars (ICP) and chambers. The numerical analysis identified the following parameters as having the most significant impact on the rock mass stability:

- Geological Strength Index (GSI), which characterizes the structural quality and strength of the rock mass;
- Chamber height, directly related to the ore body thickness;
- Excavation depth, which governs the magnitude of in-situ stresses.

A decrease in GSI—such as in fractured or poorly cemented rock masses—results in a pronounced reduction of the safety factor (SF), even when geometric parameters remain unchanged. Similarly, an increase in excavation depth elevates the overall stress state within the rock mass, leading to the expansion of failure zones and diminished pillar stability.

Thus, GSI and excavation depth are critical parameters that can cause substantial stress redistribution and a reduction in the safety margin of mining excavations. These factors must be incorporated when adapting the proposed modeling technique to other deposits, especially in conditions involving fractured or weakened rock masses.

For practical implementation across diverse geological and mining conditions, the performed sensitivity analysis facilitates the adaptation of design solutions and refinement of boundary conditions in numerical models. This approach ensures a reliable evaluation of stability and the determination of acceptable chamber-pillar system parameters tailored to the specific characteristics of each deposit. The results of this analysis are presented in Figure 21.

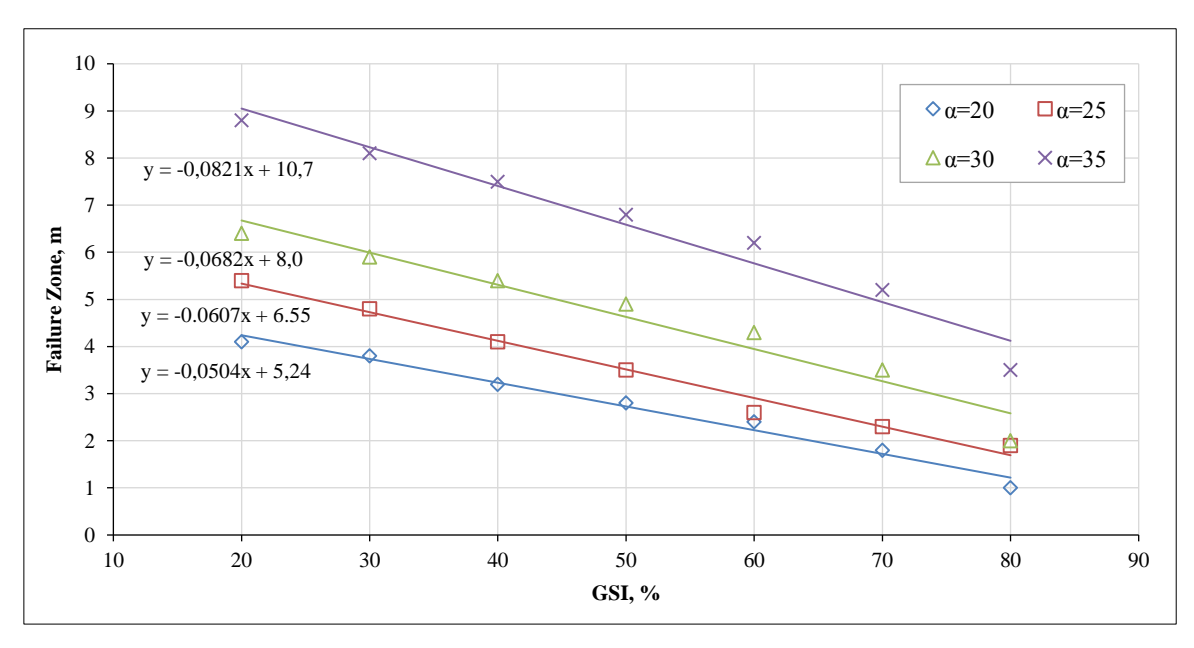


Figure 21. Analysis of the Influence of the Geological Strength Index (GSI) on the Depth of the Fracture Zone at Different Ore Body Dip Angles

The graph presented in Figure 21 illustrates the relationship between the depth of the failure zone (m) and the Geological Strength Index (GSI, %) for various ore body dip angles ($\alpha = 20^{\circ}, 25^{\circ}, 30^{\circ}$, and 35°). The analysis reveals a linear increase in the depth of the fracture zone as the GSI decreases, with the most pronounced effect observed at higher dip angles. The maximum fracture depth, reaching up to 9 m, occurs at $\alpha = 35^{\circ}$ with a GSI of approximately 20. These results indicate that the stability of the rock mass significantly deteriorates with decreasing GSI and increasing ore body dip angle.

Figure 22 shows the dependence of the failure zone depth (m) on the chamber height (m) for the same range of ore body dip angles ($\alpha = 20^{\circ}, 25^{\circ}, 30^{\circ}, \text{ and } 35^{\circ}$).

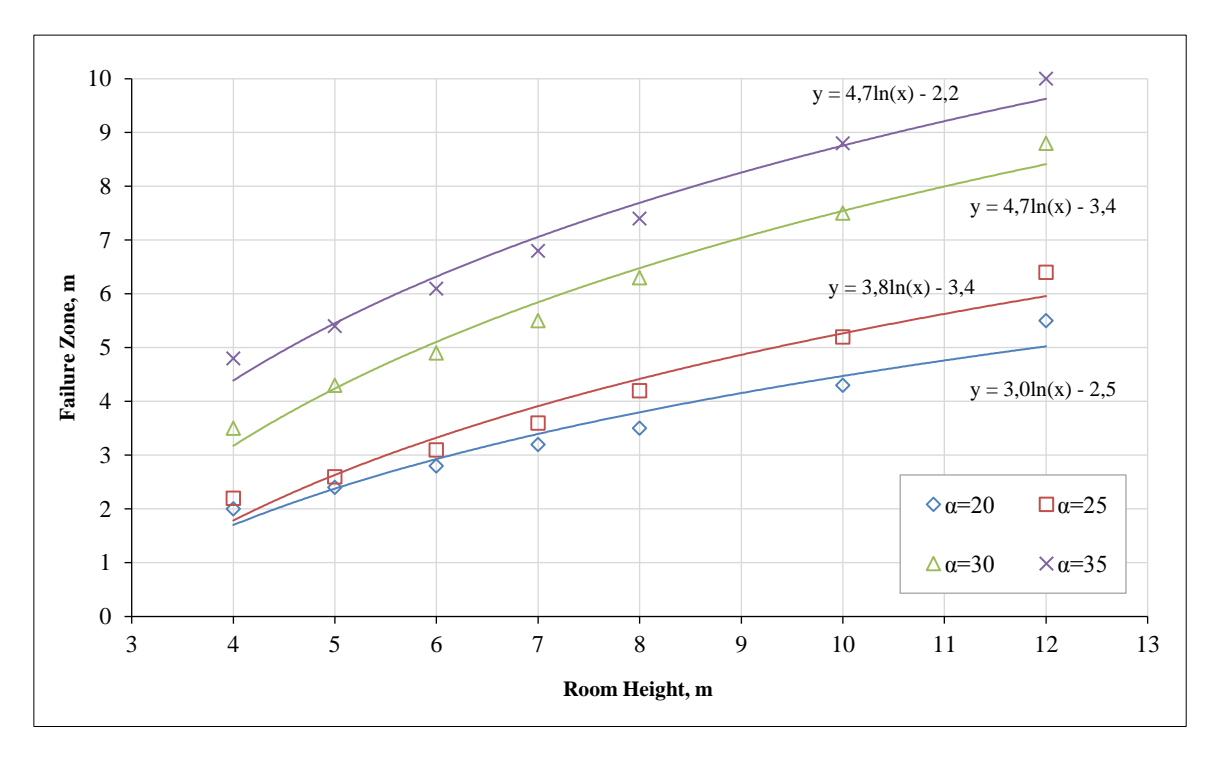


Figure 22. Influence of Chamber Height on the Depth of the Fracture Zone at Various Ore Body Dip Angles

The logarithmic relationship was identified between the chamber height and the depth of the fracture zone, indicating that as the chamber height increases, the fracture zone depth also increases, with the most pronounced effect observed at steeper dip angles. This relationship is represented by the approximation equations displayed on the graph. The maximum fracture depth, reaching up to 9 m, occurs at an ore body dip angle of $\alpha = 35^{\circ}$ and a chamber height of 12 m, highlighting a significant reduction in rock mass stability during high excavation in steeply inclined deposits.

The regression Equations further confirm that the logarithmic coefficient increases with the dip angle, demonstrating the heightened sensitivity of rock mass stability to the vertical dimensions of the excavation as the angle of incidence becomes steeper.

Numerical modeling of the stress-strain state of the rock mass enabled the determination of the principal compressive (σ_1) and tensile (σ_3) stresses, which are critical parameters in assessing rock mass stability. The principal compressive stresses indicate zones of concentrated rock pressure where the massif is most vulnerable to failure under external loads. Conversely, the principal tensile stresses identify regions prone to tension, which may result in cracking and localized damage.

The simulation was conducted at varying mining depths of 300 m, 400 m, and 500 m. The results demonstrate a consistent increase in both compressive and tensile stresses with depth, attributed to the growing rock pressure caused by the overburden load.

Figures 23 and 24 present the results of numerical modeling illustrating variations in principal compressive (σ_1) and tensile (σ_3) stresses within the rock mass as functions of mining depth and ore deposit dip angle.

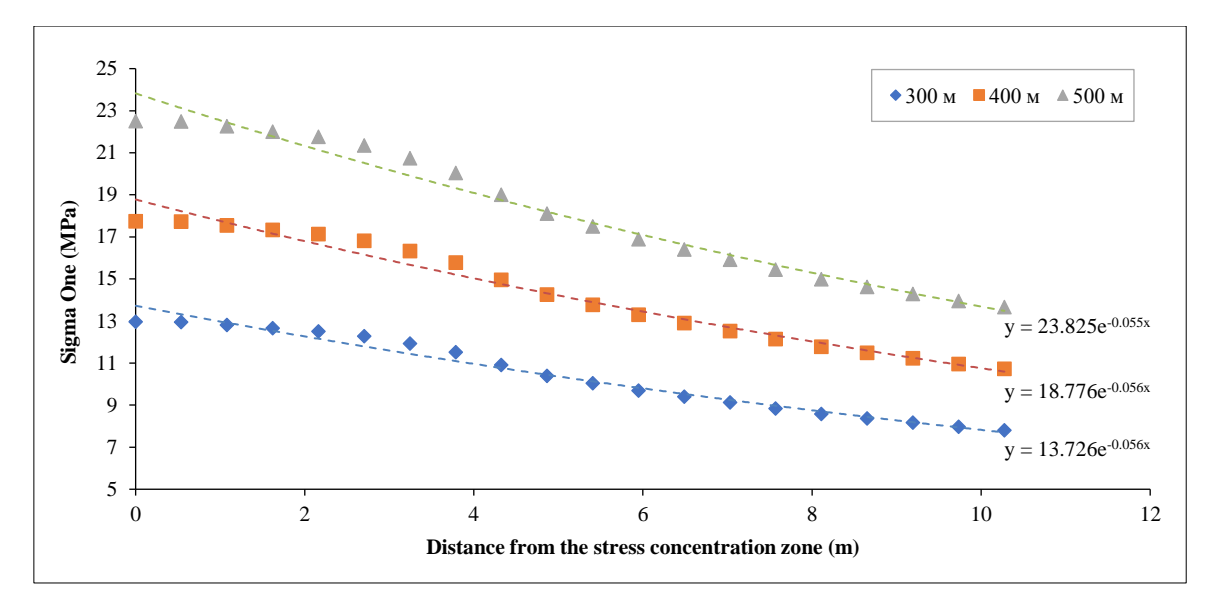


Figure 23. Graph of the Dependence of Principal Compressive Stresses (σ_1) on Mining Depth

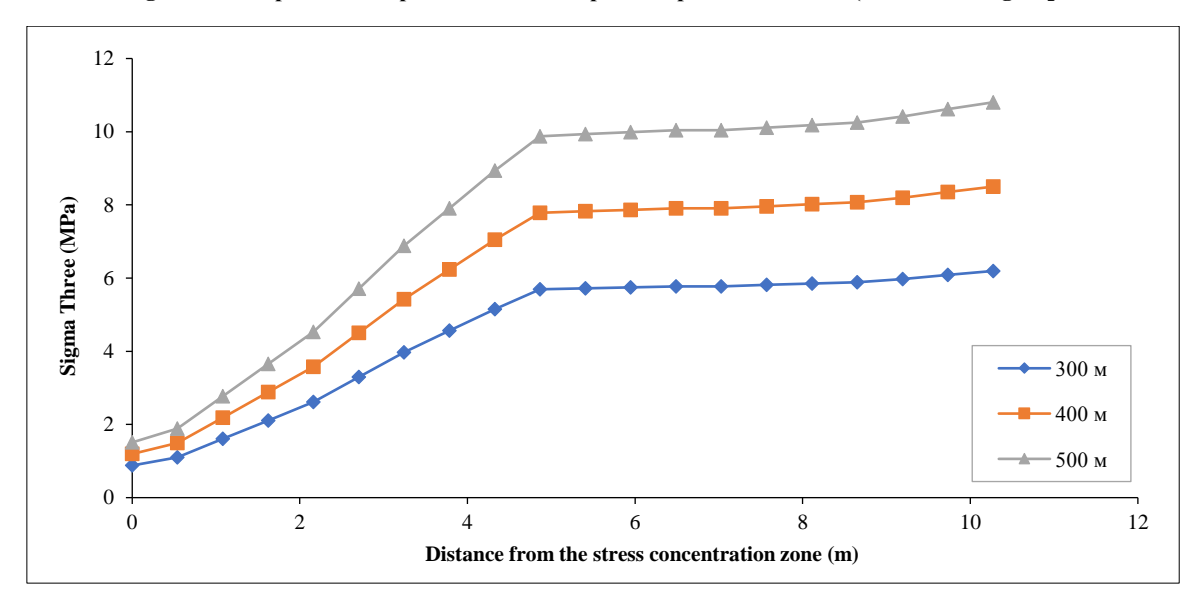


Figure 24. Graph of the Dependence of Principal Tensile Stresses (σ_3) on Mining Depth

The graphical analysis indicates a consistent increase in stress magnitudes with increasing mining depth, primarily due to the proportional rise in rock pressure exerted by the overburden. Additionally, variations in the dip angle of the ore deposits lead to stress redistribution within the rock mass, resulting in the following effects:

- Compressive stresses increase with depth, reaching peak values near the inter-chamber pillars. As the dip angle increases, zones of compressive stress concentration shift, thereby intensifying the load on the lower sections of the pillars.
- Tensile stresses also amplify with depth, particularly in the roof zones of the chambers. With increasing dip angle, tensile stress zones expand, potentially exacerbating the risk of localized collapses, especially in weaker rock formations.

Overall, the stress analysis confirms that both principal compressive and tensile stresses within the massif escalate with increasing mining depth and ore body dip angle, underscoring the importance of these factors in stability assessments.

4. Conclusion

The study was conducted at an operational field utilizing a chamber-pillar mining system, making it highly relevant for adaptation to challenging geological conditions without requiring fundamental changes to the existing mining technology. Unlike sublevel caving and other mass mining methods, the proposed approach ensures predictable stability of chambers and inter-chamber pillars through numerical modeling and geomechanical analysis. Transitioning to alternative mining systems would entail substantial investments, including equipment replacement, infrastructure

modifications, and workforce retraining, rendering such changes economically unfeasible. Therefore, modernizing the current technology allows for enhanced safety, sustained stability of workings, and system adaptability to variable structural and geological conditions with minimal production risks.

The comprehensive investigation quantified the influence of ore body dip angle, excavation geometry, and rock mass properties on the stability of the chamber-pillar system. Employing geotechnical mapping, laboratory testing, and numerical modeling, the stress-strain behavior of the rock mass was analyzed for various chamber widths and interchamber pillar dimensions. Safety margin coefficient (SF) calculations demonstrated that increasing the dip angle from 20° to 35° significantly enlarges the fracture zone depth and reduces the stability of inter-chamber pillars, especially when their width falls below 7–8 m. The relationship between fracture zone depth, chamber height, and geological strength index (GSI) follows a logarithmic trend, indicating heightened sensitivity of the rock mass to these parameters. At high GSI values (>55) and chamber heights up to 9 m, stability is preserved even with steeper dip angles. However, with a GSI decline to around 40, reducing chamber width and increasing pillar width become necessary to maintain safe working conditions.

Based on sensitivity analysis, critical geometric limits for maintaining rock mass stability were established: chamber width not exceeding 13 m and inter-chamber pillar width not less than 7 m. The use of SF = 1.2 as a stability threshold is justified and aligns with international engineering standards. These findings not only optimize development parameters for the Zhezkazgan field but also provide a framework adaptable to other mining sites with similar geomechanical characteristics. The principal advantage of the proposed methodology lies in its practical applicability, enabling parameter adjustments without fundamentally altering the mining technology—a key consideration for active operations.

5. Declarations

5.1. Author Contributions

Conceptualization Ai.M. and A.I.; methodology, Ai.M. and G.Y.; software, G.Zh. and Ai.M.; validation, A.S., G.Y., and Az.M.; formal analysis, A.I.; investigation, N.Sh; resources, G.Y.; data curation, N.Sh; writing—original draft preparation, Sh.Z.; writing—review and editing, A.I.; visualization, A.S.; supervision, Az.M.; project administration, Ai.M.; funding acquisition, G.Zh. All authors have read and agreed to the published version of the manuscript.

5.2. Data Availability Statement

The data presented in this study are available on request from the corresponding author.

5.3. Funding

This research has been funded by the Science Committee of the Ministry of Science and Higher Education of the Republic of Kazakhstan (Grant No. AP23489856).

5.4. Conflicts of Interest

The authors declare no conflict of interest.

6. References

- [1] Musin, A. A., Imashev, A. J., Shaike, N. K., Suimbaeva, A.M. (2024). Determining The Stable State of Man-Made Outbursts During Mining of Inclined Ore Deposits by Room-And-Pillar Mining. Mining Journal of Kazakhstan, 10(234), 6–12. doi:10.48498/Minmag.2024.234.10.001. (In Russian).
- [2] Dzimunya, N., Fujii, Y., Li, Z., & Amagu Amagu, C. (2025). Assessing Pillar Design Strategies in Hard Rock Room-and-Pillar Mining: A Review and Case Studies from the Great Dyke of Zimbabwe. Mining, Metallurgy & Exploration, 42(2), 685-704. doi:10.1007/s42461-025-01200-9.
- [3] Huang, Y. (2022). Numerical investigation of stress field evolution in inclined ore bodies. TUST, 134, 105008. doi:10.1016/j.tust.2022.105008.
- [4] Imashev, A. Z., Suimbayeva, A. M., Abdibaitov, S. A., Musin, A. A., & Asan, S. Y. (2020). Justification of the optimal cross-sectional shape of the mine workings in accordance with the rating classification. UGOL, 6(6), 4–9. doi:10.18796/0041-5790-2020-6-4-9.
- [5] Zhang, Y., & Ni, P. (2018). Design optimization of room and pillar mines: A case study of the Xianglushan tungsten mine. Quarterly Journal of Engineering Geology and Hydrogeology, 51(3), 352–364. doi:10.1144/qjegh2017-037.
- [6] Napa-García, G. F., Câmara, T. R., & Navarro Torres, V. F. (2019). Optimization of room-and-pillar dimensions using automated numerical models. International Journal of Mining Science and Technology, 29(5), 797–801. doi:10.1016/j.ijmst.2019.02.003.
- [7] Kumar, S., Sinha, R. K., Jawed, M., & Murmu, S. (2024). Assessment of coal pillar strength under the influence of sand stowing in deep coal mines. Geotechnical and Geological Engineering, 42(4), 2815–2831. doi:10.1007/s10706-023-02707-y.

- [8] Zhou, Z., Zhou, J., Lai, L., Xu, M., & Xu, Y. (2024). Determination of optimal mining width for coal mining under the slope by of using numerical simulation. Scientific Reports, 14(1), 1124. doi:10.1038/s41598-024-51624-4.
- [9] Wu, Y., Tang, Y., Xie, P., Hu, B., Lang, D., & Wang, H. (2024). Stability analysis of 'roof-coal pillar' structure in longwall multi-section mining of steeply dipping coal seam. Geomatics, Natural Hazards and Risk, 15(1). doi:10.1080/19475705.2024.2359998.
- [10] Pan, Q., & Dias, D. (2018). Three dimensional face stability of a tunnel in weak rock masses subjected to seepage forces. Tunnelling and Underground Space Technology, 71, 555–566. doi:10.1016/j.tust.2017.11.003.
- [11] Martin, C. D., & Maybee, W. G. (2000). The strength of hard-rock pillars. International Journal of Rock Mechanics and Mining Sciences, 37(8), 1239-1246. doi:10.1016/S1365-1609(00)00032-0.
- [12] He, Y., Huang, Q., & Ma, L. (2024). Research on roof weighting mechanism of coal pillar mining in shallow buried closely spaced multi-seams. Lithosphere, 2024(3), 109. doi:10.2113/2024/lithosphere_2024_109.
- [13] Eremin, M., Peryshkin, A., Esterhuizen, G., Pavlova, L., & Fryanov, V. (2022). Numerical Analysis of Pillar Stability in Longwall Mining of Two Adjacent Panels of an Inclined Coal Seam. Applied Sciences (Switzerland), 12(21), 11028. doi:10.3390/app122111028.
- [14] Eremenko, V. A., Kosyreva, M. A., Vysotin, N. G., & Khazhy-Ylai, C. V. (2021). Geomechanical justification of room-and-pillar dimensions for rock salt and polymineral salt mining. Gornyi Zhurnal, 2021(1), 37–43. doi:10.17580/gzh.2021.01.07.
- [15] Ma, T., Wang, L., Suorineni, F. T., & Tang, C. (2016). Numerical Analysis on Failure Modes and Mechanisms of Mine Pillars under Shear Loading. Shock and Vibration, 2016, 6195482. doi:10.1155/2016/6195482.
- [16] Sordo, B., Rathje, E., & Kumar, K. (2024). Sequential hybrid finite element and material point method to simulate slope failures. Computers and Geotechnics, 173, 106525. doi:10.1016/j.compgeo.2024.106525.
- [17] Quevedo, R. J., Sari, Y. A., & McKinnon, S. D. (2024). Cave mine pillar stability analysis using machine learning. Journal of the Southern African Institute of Mining and Metallurgy, 124(2), 43–52. doi:10.17159/2411-9717/2509/2024.
- [18] Vlachogiannis, I., & Benardos, A. (2024). Proposed formulas for pillar stress estimation in a regular room-and-pillar pattern. International Journal of Rock Mechanics and Mining Sciences, 180, 105826. doi:10.1016/j.ijrmms.2024.105826.
- [19] Mehra, A., & Budi, G. (2024). 3D Modelling approach to identify parametric configurations for pillar stability in underground metal mine: a case study. Geomatics, Natural Hazards and Risk, 15(1), 2367630. doi:10.1080/19475705.2024.2367630.
- [20] Maina, D., & Konietzky, H. (2025). The effect of the intermediate principal stress on pillar strength. International Journal of Coal Science & Technology, 12(1), 8. doi:10.1007/s40789-025-00747-8.
- [21] Imashev, A. Zh., Sudarikov, A. E., Musin, A. A., Suimbayeva, A. M., & Asan, S. Yu. (2021). Improving the Quality of Blasting Indicators by Studying The Natural Stress Field and The Impact of the Blast Force on The Rock Mass. Series of Geology and Technical Sciences, 4(448), 30–35. doi:10.32014/2021.2518-170x.78.
- [22] Mussin, A., Kydrashov, A., Asanova, Z., Abdrakhman, Y., & Ivadilinova, D. (2024). Ore dilution control when mining low-thickness ore bodies using a system of sublevel drifts. Mining of Mineral Deposits, 18(2), 18–27. doi:10.33271/mining18.02.018.
- [23] Imashev, A. Z., Suimbaeva, A. M., & Musin, A. A. (2024). Predictive assessment of ore dilution in mining thin steeply dipping deposits by a system of sublevel drifts. Notes of the Mining Institute, 266, 283-294.
- [24] Hoek, E., & Brown, E. T. (2019). The Hoek–Brown failure criterion and GSI 2018 edition. Journal of Rock Mechanics and Geotechnical Engineering, 11(3), 445–463. doi:10.1016/j.jrmge.2018.08.001.
- [25] Fisher, R. (1953). Dispersion on a Sphere. Proceedings of the Royal Society A: Mathematical, Physical and Engineering Sciences, 217(1130), 295–305. doi:10.1098/rspa.1953.0064.
- [26] Terzaghi, R. D. (1965). Sources of error in joint surveys. Geotechnique, 15(3), 287-304. doi:10.1680/geot.1965.15.3.287.
- [27] Barton, N., Lien, R., & Lunde, J. (1974). Engineering classification of rock masses for the design of tunnel support. Rock Mechanics Felsmechanik Mécanique Des Roches, 6(4), 189–236. doi:10.1007/BF01239496.
- [28] Hoek, E., Marinos, P., & Benissi, M. (1998). Applicability of the geological strength index (GSI) classification for very weak and sheared rock masses. The case of the Athens Schist Formation. Bulletin of Engineering Geology and the Environment, 57(2), 151–160. doi:10.1007/s100640050031.
- [29] Gavin, H. P. (2019). The Levenberg-Marquardt algorithm for nonlinear least squares curve-fitting problems. Department of Civil and Environmental Engineering Duke University August, 3, 1-23.
- [30] Yue, R., Li, K., Qin, Q., Li, M., & Li, M. (2022). Study on the Weakening Law and Classification of Rock Mass Damage under Blasting Conditions. Energies, 15(5), 1809. doi:10.3390/en15051809.